UNIVERSITÀ DEGLI STUDI DI CATANIA
Dipartimento di Fisica e Astronomia
Dottorato di Ricerca in Fisica
XXX Ciclo

---

Mariarita Murabito

# ANALYSIS OF THE PENUMBRA FORMATION IN SUNSPOTS

---

Tesi di Dottorato

---

Coordinatore: Prof. V. Bellini

Tutor: Chiar.ma Prof.ssa F. Zuccarello

Cotutors: Dott. P. Romano
Dott. S. L. Guglielmino

---

anno accademico 2016/2017

# Contents

# Abstract

The formation of the penumbra in sunspots is a physical process which involve the coupling between the plasma and the magnetic field in different layers of the solar atmosphere. Its study requires long time series of observations carried out with high temporal, spatial, and spectral resolution. Moreover, due to few available datasets of this phase of the sunspot evolution, the physical processes at the base of the penumbra formation are still unclear. For this reason in this thesis I performed some observational analysis of the penumbra formation using high resolution data acquired during an observing campaign at the Richard B. Dunn Solar Telescope (NSO) and data taken by HMI onboard of SDO.

Two main aspects have been investigated: the location of the stable settlement of the first penumbra filaments and the transition from inverse to classical Evershed flow.

Using the high resolution images I observed the first settlement of the penumbra filaments in the two polarities of AR NOOA 11490. Before the penumbra formation the pore of the preceding polarity exhibits an annular zone characterized by a

magnetic field greater than 1000 G, having an (upside down) ballerina skirt structure of the magnetic field. In this case, the penumbra starts to form in the side away from the opposite polarity, in agreement with the observations of Schlichenmaier et al. (2010). On the other hand, using the same dataset, I showed that in the following polarity of the AR NOAA 11490 a stable penumbra forms in the area facing the opposite polarity, located below an AFS, i.e. in a flux emergence region.

Moreover, considering a sample of other six ARs observed by HMI, I found that there is no preferred location for the penumbra formation.

I interpreted the formation of the penumbra as due to the field lines of the magnetic canopy, already existing at a higher level of the solar atmosphere and overlying the pore, which sink down into the photosphere and below the solar surface. In fact, in this case there is a non-zero probability of finding near-horizontal field also in the region between the two main sunspots, as shown by the recent simulations of MacTaggart et al. (2016).

Concerning the transition from inverse to classical Evershed flow, in the preceding polarity of AR NOAA 11490 I found changes in the direction of the LOS velocity field during the formation of the first penumbral sector. In about 1-3 hours the LOS velocity became coherent with the Evershed flow pattern while the penumbra was completely formed. I also found observational evidences of this transition in most of the pores of my

sample observed by HMI. Therefore, I proposed a new model to explain this transition in the velocity field, based on the presence of small U-loops, which are able to drive a siphon flow toward the pore, i.e., corresponding to the inverse Evershed flow, before the penumbra formation.

The thesis is organized as follows: in Chapter 1 I provide a brief introduction on the characteristics of the solar active regions. Chapter 2 describes the main features observed in solar sunspots with particular attention to the penumbra and its formation, taking into account both the observational and theoretical point of view. The used instruments, the data and their method of analysis have been described in Chapter 3. Chapters 4 and 5 report the analysis of the data concerning the preceding and following polarities of AR NOAA 11490, respectively. The study carried out using a sample of 6 ARs observed by HMI is reported in Chapter 6. A discussion containing a possible scenario for the penumbra formation and the transition from the inverse to the classical Evershed flow is reported in Chapter 7. The conclusions drawn from the results obtained in this thesis are reported in Chapter 8.

# Chapter 1

# Introduction

## 1.1 Solar Active Region morphology and evolution

---

Active regions (ARs) are defined by the totality of observable phenomena from the photosphere to the corona as a result of the magnetic flux emerged from the convection zone, revealed by emissions over a wide range of wavelengths from radio to X-rays (van Driel-Gesztelyi & Green, 2015). The simplest ARs have a bipolar magnetic field configuration, but usually ARs may be built-up due to several bipoles emerging in close succession. Bipolar ARs are usually aligned in the east-west direction and for the Hale's law they have opposite leading magnetic polarities on opposite hemisphere.

In the photosphere the presence of a strong magnetic field

is manifested by the appearance of dark sunspots or pores[1] and bright faculae representing concentrated and diffused magnetic fields, respectively. In the chromophere ARs are charcterized by the presence of arch filament systems (AFSs), filaments and bright regions called plages. The AFS are bundles of dark arches crossing the polarity inversion line (PILs) (Bruzek, 1968). The dark filamentary structures observed on the solar disk, called filaments, are due to dense and cold plasma suspended in the extremely hot corona. They are found above the PILs (Wang et al., 2017).

In the upper layers, i.e. transition region and corona, we observe that the magnetic opposite polarities are connected by bright, dense and hot loops. In figure 1.1 we show an example of ARs in photosphere, chromosphere and corona.

### 1.1.1 Mount Wilson classification

There are many classifications useful to describe the AR morphology. Here I report the Mount Wilson magnetic classification that describes the magnetic complexity of sunspot groups in photosphere:

$\alpha$ - Unipolar sunspot group.

[1]The presence of a penumbra distinguishes sunspots from pores

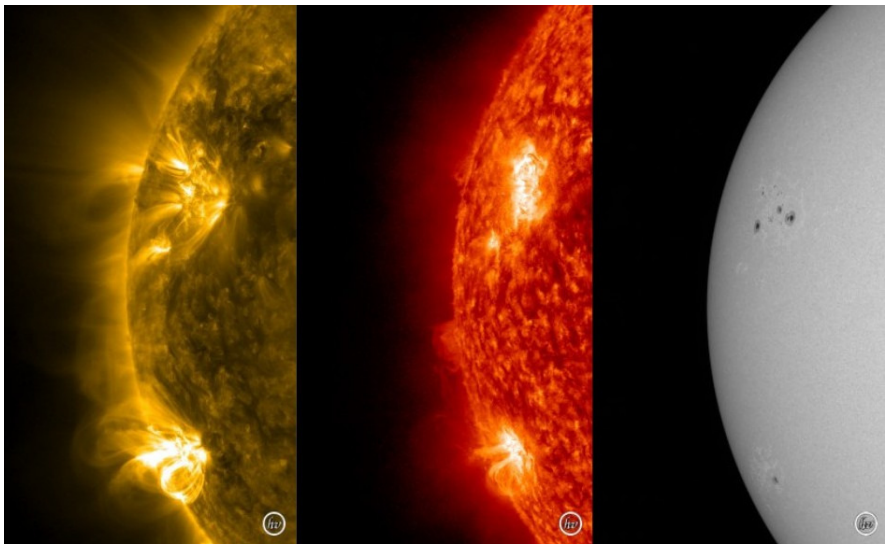

Figure 1.1: Active regions on the solar disk. From left to right: corona, chromophere and photosphere, respectively. SDO

$\beta$ - A sunspot group with distinct and well separated positive and negative magnetic polarities.

$\beta$-$\gamma$ - A bipolar sunspot group where the spots of opposite polarity are not well separated.

$\gamma$ - A sunspot group where the distribution of positive and negative magnetic polarity is irregular.

$\delta$ - A sunspot group with complex magnetic configuration, consisting of opposite polarity umbrae within the same penumbra.

### 1.1.2 Evolution of ARs

---

The magnetic flux tubes of the toroidal magnetic field generated by the dynamo in the tachocline, are called $\Omega$ loops. During their rise from the convection zone into the upper layers of the solar atmosphere they are influenced by the Coriolis force, magnetic tension, drag, plasma vortices and large-scale convective motions. Figure 1.2 shows a sketch of a flux tube that is rising from the convective zone.

When the magnetic flux tubes reach the photosphere, we observe a nearly horizontal, upward-moving ($\approx 1$ kms$^{-1}$) magnetic field with strength of 200-600 G. The individual flux elements at photospheric level move rapidly away from the emergence site and, when the magnetic field becomes nearly vertical, its

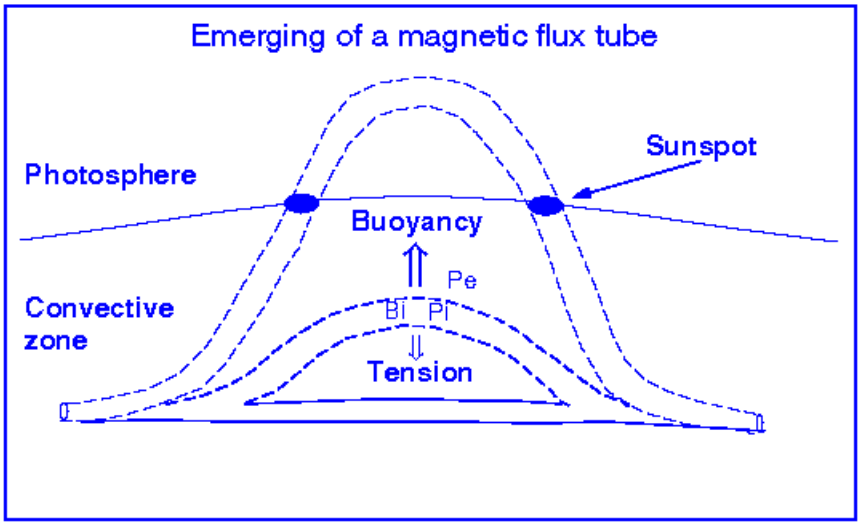


Figure 1.2: Sketch of a magnetic flux tube rising from the convective zone. $B_i$ indicates the magnetic field strength of the magnetic flux tube, Pi and Pe are the gas pressures inside and outside the flux tube at the same height, respectively.

strength reaches values of kG. During this phase the granulation pattern is anomalous, i.e. the granules between the opposite polarities become larger and elongated (Guglielmino et al., 2010). When the top of magnetic flux tubes emerges through the photosphere, between the two opposite polarity flux concentrations (pores and spots) dark inter-granular lanes appear, being characterized by a lifetime of 10-30 minutes (van Driel-Gesztelyi & Green, 2015).

The bipolar magnetic field expands and bright plages appear. The configuration of the magnetic field starts to change, becoming a mixture of weak horizontal and more vertical field. On small scale, the magnetic field appears like serpentine, i.e. undulatory flux formed by an alternative series of small $\Omega$ and U-loops that cross the photosphere (Watanabe et al., 2008). Then an AFS appears in H$\alpha$ images. Individual arches are short-lived (20-30 minutes), but the AFS exists as long as flux is emerging (van Driel-Gesztelyi & Green, 2015). Right above the AFS we observe hot and brigth EUV and X-rays loops (Kawai et al., 1992; Malherbe et al., 1998). In this phase, usually, the photospheric magnetic field reaches values of 2000-2500 G due to the convective collapse (Parker, 1978), where plasma drain out of the rising loops, increasing the strength of the magnetic field (Zwaan et al., 1985; Lites et al., 1998).

The same-polarity concentrations form pores that move towards each other and coalesce forming sunspots. The formation

of the penumbra around a pore is part of the flux emergence process. The emerging flux starts reconnecting with the surrounding pre-existing fields forming new coronal magnetic connections. During the flux emergence process, we observe a high flare rate, but the flare number peaks when the sunspot area of the AR reaches its maximum.

When no new magnetic flux emerges anymore through the photosphere, the AR starts decaying. We observe, in this stage, small magnetic flux concentrations (MMFs) that move away from the sunspots. The first decaying signature in the sunspot evolution is the appearance of light bridges (LBs). Figure 3.1 shows the evolution of a sunspot and the formation of the LB. Usually, the flare activity decreases after a solar rotation, but the number of coronal mass ejections (CMEs) coming form the AR does not seem to decrease. In this phase, although the emission of chromospheric plages is still high, the magnetic field density decreases. Faint emission is revealed in the corona except for X-ray bright points related to the emergence and cancellation of smaller-scale flux (Sheeley, 1981; Schrijver & Zwaan, 2000; Harvey & Zwaan, 1993). Finally, the enhanced network disappears and the AR loses its identity.

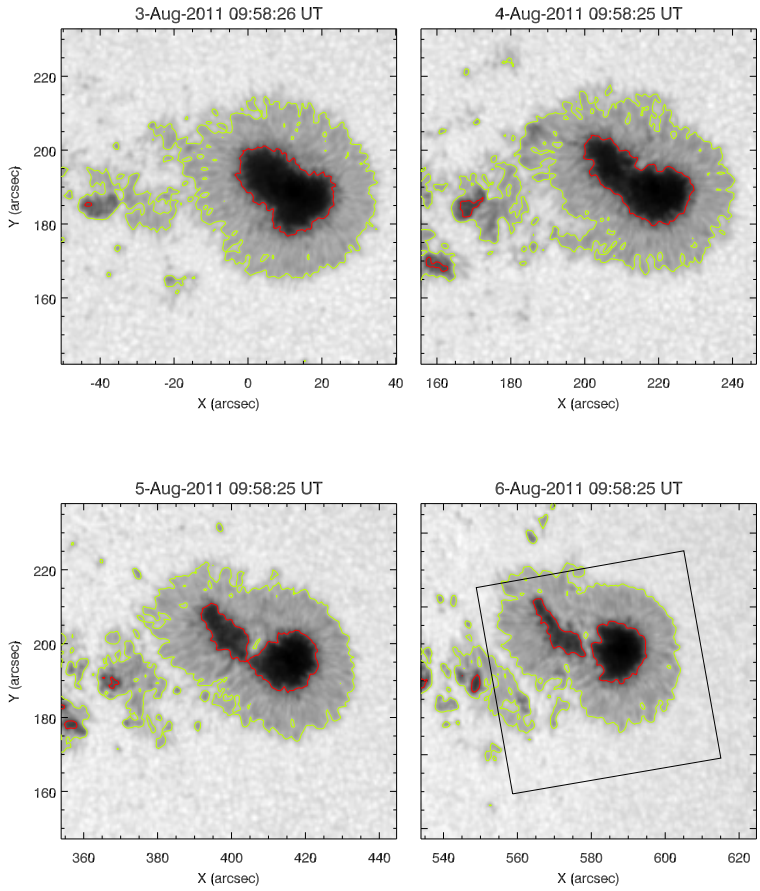


Figure 1.3: HMI/SDO images in the continuum of the preceding sunspot of NOAA AR 11263. The sequence shows the evolution of the sunspot umbra and the formation of a light bridge (Falco et al., 2016).

# Chapter 2

# Sunspots: observations and models

Sunspots are the most prominent manifestation of magnetic flux emergence in the photosphere. The sunspot properties have been studied since their first observation (1610, Galileo and Steiner, Solanki (2003)) and their discover as locations of strong magnetic field (Hale, 1908). Our understanding of sunspots increases with the new facilities developed both for high resolution observations and MHD simulations.

## 2.1 Sunspot physical parameters

Sunspots are dark structures in the solar photophere. They are composed of an inner dark area, the umbra, and an outer less dark region with a filamentary structure: the penumbra. The magnetic field inhibites the convective flows, i.e. it supppresses the heat transport by convection, and for this reason sunspots are cooler than the surrounding solar photophere where the average heat flux of $6.31\times10^7$ W/$m^2$. Consequently the heat flux is reduced by 25% and 77% in the penumbra and the umbra, respectively (Rempel & Schlichenmaier, 2011). The effective temperature that corresponds to these heat fluxes are $\sim$ 5777 K, $\sim$ 5275 K and $\sim$ 4000 K for quiet Sun, umbra and penumbra, respectively.

Sunspots exhibit a broad size distribution, even if smaller sunspots are more common than larger ones. The size varies between 3500 km and 60000 km, from the smallest to the biggest ones (Solanki, 2003). Sunspots can have lifetimes of months or only hours. In general the sunspots lifetime depends on the sunspot size. The following rule was formulated for the first time by Waldmeier in 1955: $A_0 = WT$, where $A_0$ is the mazimum size of the spot, T the lifetime and W is a constant recently found to be equal to $1089\pm0.18$ MSH $day^{-1}$ (MSH, Millionths of the Solar Hemiphere) according to Petrovay & van Driel-Gesztelyi (1997). The magnetic field is almost vertical in the central part of the

umbra, where it varies from 1800 G to 3700 G, while it decreases from the inner part to the outer edge of the penumbra, reaching values between 700-1000 G. In the penumbra the magnetic field is more inclined.

The number and the location of sunspots varies over the solar cycle. During the minimum it is possible that no sunspots are visible on the solar surface, while during the maximum it is usual to see 10 or more groups of sunspots. Usually they appear in a belt between $+30°$ and $-30°$ from the solar equator. Carrington in 1863 noticed that the sunspots location is not casual, but when the solar cycle starts, sunspots appear at high latitudes, sometimes up to $40°$ from the solar equator. During the cycle, sunspots appear at lower latitudes and at the end of the cycle they are very close to the equator. This behavior is well described by the so called 'butterfly diagram', shown in Figure 2.1.

### 2.1.1 Fine structure of sunspots

In the last 50 years space and ground-based observations have highlighed the dynamic and fine structure of the sunspots. Despite the fact that sunspots are globally stable, a variety of small-scale features such as umbral dots (UDs), light bridges (LBs), bright and dark penumbral filaments, appear in the sunspots and evolve on a dynamic time scale.

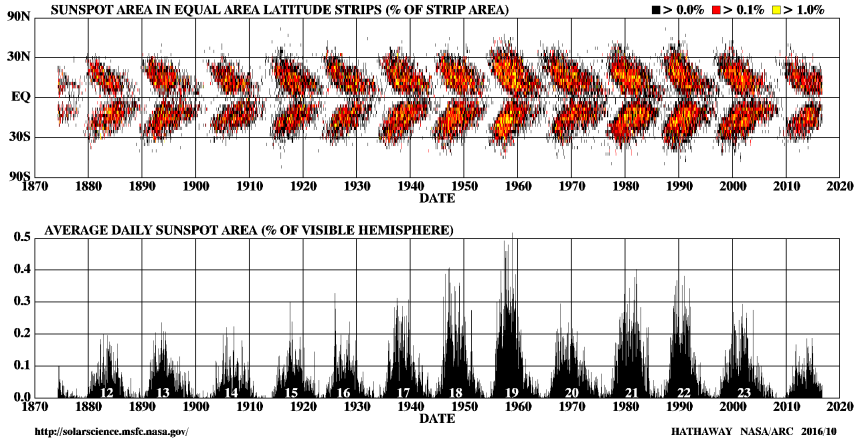


Figure 2.1: Butterfly diagram for the years 1874-2016, NASA

### Umbral dots (UDs)

Umbral dots were observed for the first time in 1964 by Danielson (1964) as bright dot-like spots inside the umbra, with typical size less than $0\farcs5$ (see left panel of Figure 2.2). Although the UDs seem to be present in all sunspots, there is not a typical intensity value in photophere (Rempel & Schlichenmaier, 2011). From the observations it has been possible to estimate a temperature difference between them and the umbral background that ranges between 500 K and 1500 K at $\tau = 2/3$[1] (Borrero & Ichimoto, 2011). It is possible to distinguish two types of UDs: central umbral dots (CUDs), which appear close to the darkest region

[1] $\tau$ corresponds to the optical depth defined as $d\tau = \kappa ds$, where $\kappa$ is the absorption coefficient and s is the geometrical coordinate.

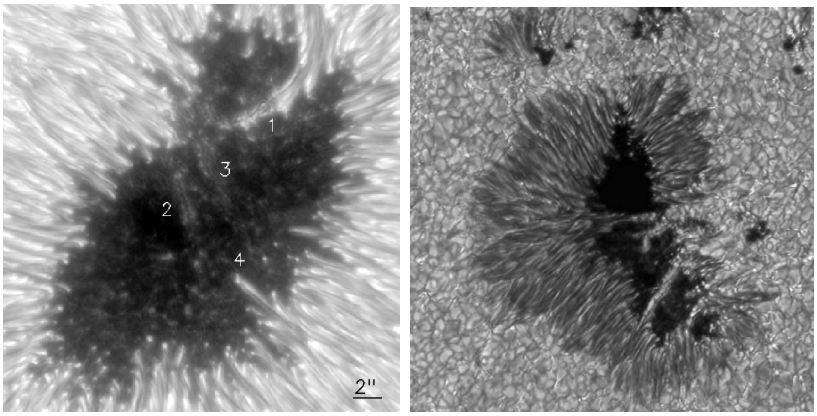


Figure 2.2: Left panel: NOAA 10634 with LBs and UDs (Sobotka & Puschmann, 2009). Right panel: Complex sunspot crossed by several LBs (Solanki, 2003)

of the umbra and peripheral umbral dots (PUDs), which appear at the umbral and penumbral boundary (Borrero & Ichimoto, 2011).

Despite the study of the magnetic field in UDs has been really controversial, it seems that it is weaker than in the surroundings: it is $10\% - 20\%$ lower in CUDs and $5\% - 10\%$ lower in PUDs (Schmidt & Balthasar, 1994). The lower magnetic field inside UDs is a direct consequence of the convective motions. In fact, the magnetic field lines in the umbra are pushed by the convective motions towards the edge of the convective cell, creating a region where the vertical component of the magnetic field vector is strongly reduced (Borrero & Ichimoto, 2011).

### Light bridges (LBs)

Light bridges are bright and elongated features that cross the umbra. The right panel of Figure 2.2 shows an image of a complex sunspot with four LBs crossing the umbra.

LBs have a significantly lower magnetic field strength with respect to the umbra, with a reduction ranging from 200 to 1500 G (Leka, 1997). In addition to that, the magnetic field is more inclined, between 5° and 30° larger than in the umbra (Solanki, 2003).

### Penumbral filaments

The penumbra is composed by dark and bright filaments and penumbral grains (see Figure 2.2). High spatial resolution observations have shown small features in the penumbral filaments, which appear uniform at resolution worse than $1''$[2]. At high spatial resolution it can be seen that intensity, velocity field and magnetic field values indicate a filamentary structure (Rempel & Schlichenmaier, 2011). The filaments have a tipical width, according to Scharmer et al. (2002), of $0''.2$ - $0''.25$ in the continuum images. The dark and the bright filaments are characterized by a continuum intensity of $\sim 0.3 - 0.7\, I_c$ and $\sim 0.7 - 1.0\, I_c$, respectively (Muller, 1973).

The magnetic field consists of two components: *spines* and *intraspines*. The magnetic field is stronger and more vertical

[2] $1''$ corresponds to 728 km on the solar surface

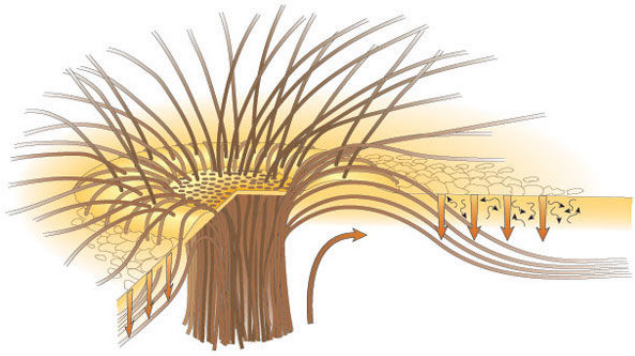

Figure 2.3: Sketch showing the interlocking-comb structure of the magnetic field in the filamentary penumbra of a sunspot (Thomas et al., 2002).

with respect to the solar surface in the spines, while the intraspines are characterized by a magnetic field weaker and more horizontal (Borrero & Ichimoto, 2011). This magnetic field configuration is referred as 'interlocking comb' structure (Thomas & Weiss, 1992) or 'uncombed penumbra' (Solanki & Montavon, 1993) (Figure 2.3).

The magnetic field lines of the spines are connected with regions far from the sunspots, to form coronal loops over the active region, while the magnetic field lines of the intraspines turn back into the photosphere at the edge of the sunspot to form a canopy (Borrero & Ichimoto, 2011).

A possibile scenario that explains how the magnetic field lines return back into the solar surface at the edge of the penumbra

(intraspines) was formulated by Thomas et al. (2002). The key idea is that the outer part of the flux tubes are submerged by the downward pumping of the granular convection outside the sunspot, forming the low-laying horizontal flux tubes (Borrero & Ichimoto, 2011).

There are two models that try to explain the penumbra structure:

- Embedded flux tube model: this empirical model, shown in Figure 2.4, was proposed by Solanki & Montavon (1993). In this case horizontal magnetic flux tubes (intraspines) are embedded in more vertical magnetic fields (spines).

- Field free gap model: the penumbral bright filaments represent a protusion of non-magnetized, hot gas into the background oblique magnetic fields of the penumbra. In Figure 2.5 a sketch of this model is shown. The left panel corresponds to the model for an umbral dot, where the cusp is located below $\tau = 1$. The surface around the gap is bright because of the radiative heat flux. The observed field strength is reduced due to the displacement of field lines by the gap. In the middle panel we see the configuration for a light bridge, where a wide gap would be seen as a field-free canal. Finally, the right panel illustrates the situation for the penumbral filament. The sketch is similar to that shown for the light bridge, but with an additional

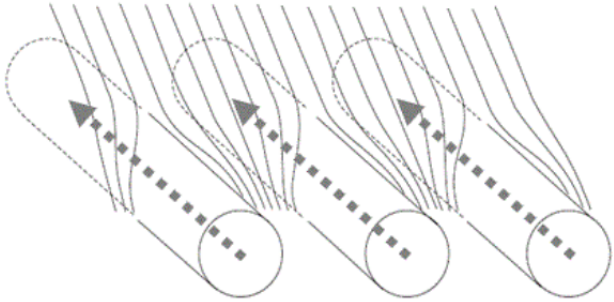

Figure 2.4: Embedded flux tube model (Borrero & Ichimoto, 2011). The solid lines indicate the vertical magnetic field (spines) while the cylindrical structures the horizontal ones (intraspines). Dashed arrows indicate the direction of the flow.

horizontal field component (indicated by shading) along the filament.

The penumbra brightness is equal to 70% - 80% of the quiet Sun granulation. An important question is how the energy transport takes place to allow this brightness. The more efficient mechanism is surely the convection, but how does the convective motions in the presence of a strong (B$\approx$ 1500 G) and horizontal ($\gamma$ $\approx$40-80°) magnetic field occur? The heat transport in the aforementioned feld-free gap model is very efficient because the convective motions are localized over the entire length of the bright filaments, with upflows at the center of the filaments and downflows at the filaments' edges. This model predicts only

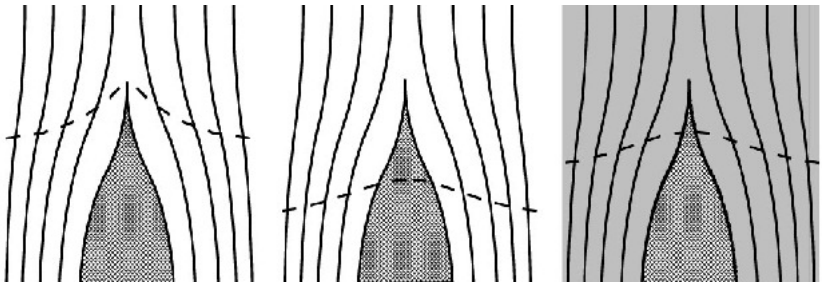

Figure 2.5: Sketch of the field-free gap model where gaps in a magnetic field near the solar surface (vertical cross-sections) are shown. Dashed lines indicate the continuum $\tau = 1$ level. The two neighboring flux bundles spread out horizontally above the surface, forming a cusp at some height above $\tau = 1$ (Spruit & Scharmer, 2006).

alternating upflows/downflows in the perpendicular direction to the filaments, azimuthally around the penumbra. For this reason this type of convection is referred to as azimuthal convection or overturning convection (see lower panel of Figure 2.6). A less efficient mechanism is represented by the hot rising flux-tube model, where the inner footpoints of the flux tube are characterized by upflows and the outer footpoints by downflows (Schlichenmaier, 2002). This type of convection is called radial convection, because the convective flows occur along the penumbral filaments (see the upper panel in Figure 2.6)

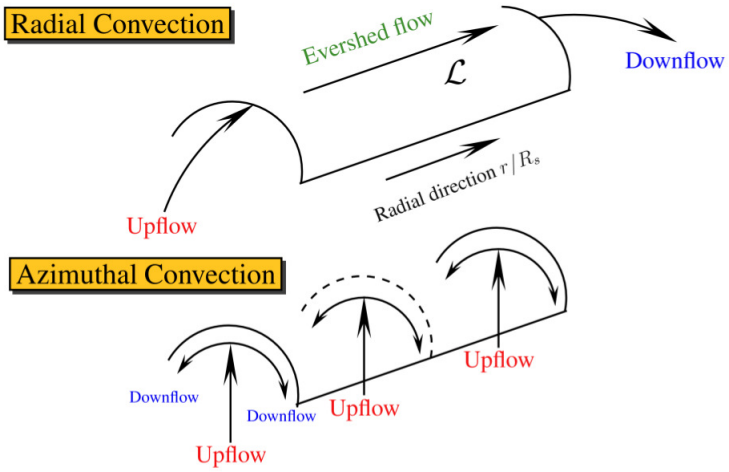


Figure 2.6: Different patterns of convection in penumbral filaments. Upper panel: radial convection predicted by the hot rising flux-tube model and the embedded flux-tube model. Bottom panel: azimuthal convection or overturning convection predicted by the field-free gap model (Borrero & Ichimoto, 2011).

## 2.2 Evershed flow

The Evershed flow is observed as a wavelength shift (red or blue) in the spectra of absorption lines in the penumbra (limb-side or disk-center). It was discovered by Evershed (1909) and can be explained by a nearly horizontal outflow in the penumbra. It seems a stationary flow, observed at insufficient spatial resolution, with a typical velocity of $\sim$ 1-2 $\mathrm{km\,s^{-1}}$.

Since 1960s it was accepted that this flow is not spatially uniform, but it is concentrated in narrow channels in the penumbra.

Until 1990, two models were proposed to explain the filamentary structure of the penumbra and the Evershed flow. Both models assumed a nearly horizontal magnetic field in the penumbra, but today this is not anymore supported by the observational evidence that a significant fraction of sunspot's vertical magnetic field is found in the penumbra (Borrero & Ichimoto, 2011). The discovery of the interlocking comb structure of the penumbra magnetic field solved the enigma on the Evershed flow. It seems in fact that the Evershed flow (middle panel of Figure 2.7) is correlated with regions where the magnetic field is horizontal (intraspines with $\gamma \approx 90°$, bottom panel of Figure 2.7) and weaker (upper panel of Figure 2.7).

The embedded flux-tube model (Solanki & Montavon, 1993) tries to explain the Evershed flow, assuming that it is confined in the horizontal magnetic flux tubes embedded in a more vertical

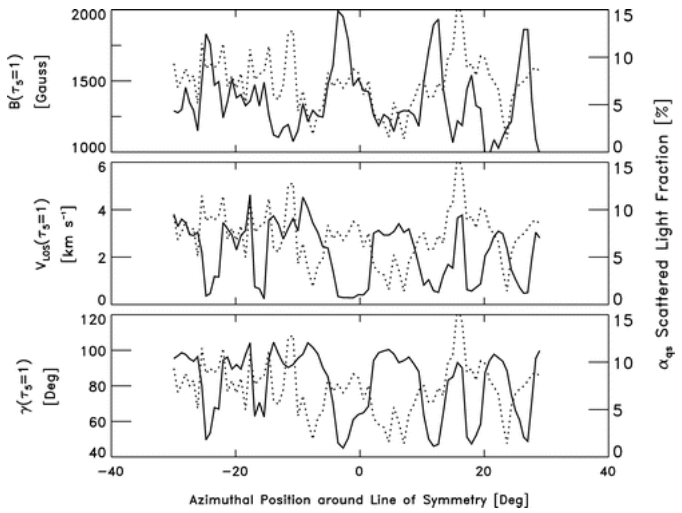


Figure 2.7: From top to bottom: Variation of the magnetic field strength B, line-of-sight velocity $V_{los}$ and inclination angle of the magnetic fiel $\gamma$ at $\tau = 1$ (continuum) along an azimuthal cut around the limb-side penumbra. Dotted curves in each panel indicate the scattered light fraction obtained from the inversion algorithm (Borrero & Solanki, 2008).

background. Within this model, the *siphon flow* mechanism was proposed as the driver of the Evershed flow. The difference of gas pressure between the two footpoints of the flux tube is caused by a difference in the magnetic field strength. This difference of gas pressure drives the flow towards the footpoints with a higher field strength (Meyer & Schmidt, 1968; Thomas, 1988; Thomas & Montesinos, 1993).

After the 1990s, clear evidence that the Evershed flow pos-

sesses a vertical component was found. In particular, the relationship between the magnetic field vector and the vertical flow in the penumbra were clearly demonstrated by spectropolarimetric data. Figure 2.8 highlights this relationship for a spot near the disk center. The V maps, (see Chapter 5.1) at ±300 mÅ show two different patterns: in the -300 mÅ V map, small and elongated structures with the same polarity of the sunspot are visible in the inner penumbra, while in the +300 mÅ V map, patches of opposite polarity of the sunspot are seen in the mid and outer penumbra. These features are associated with upward (1 $\mathrm{km\,s^{-1}}$) and downward motions (∼4-7 $\mathrm{km\,s^{-1}}$), respectively (bottom panels in Figure 2.8) (Borrero & Ichimoto, 2011).

Taking into account the results concerning the velocity field and the magnetic field vector, it is possible to draw a picture of the penumbra as shown in Figure 2.9.

Even if the relationship between the Everhed flow and the intensity of the penumbra has been controversial, recent observations demonstrate that the Evershed flow takes place in the bright filaments in the inner penumbra and in the dark filaments in the outer penumbra (Schlichenmaier et al., 2005; Bellot Rubio et al., 2006; Ichimoto et al., 2007).

One aspect however needs to be further investigated: the relationship between the penumbra formation and the estabilishment of the Evershed flow. Schlichenmaier et al. (2012) revealed, before the penumbra formation, a line of sight (LOS) velocity of

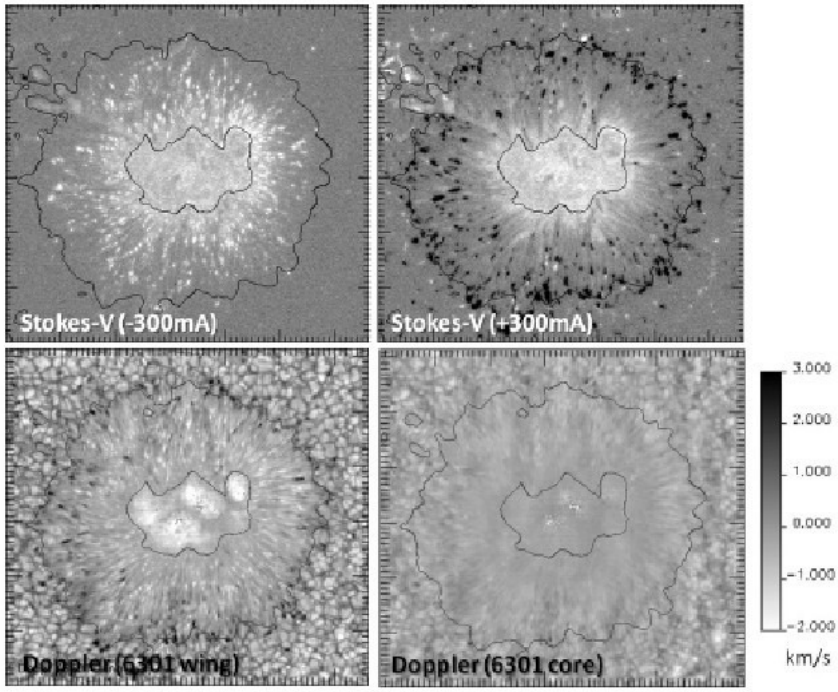


Figure 2.8: Upper and middle panels: Stokes V maps of a sunspot. Bottom panel: Doppler velocity (Borrero & Ichimoto, 2011).

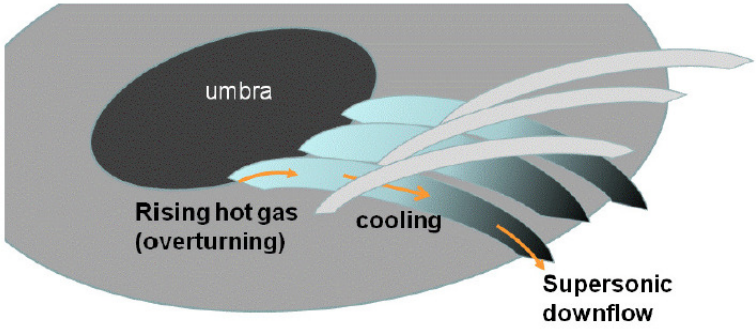


Figure 2.9: Cartoon of the penumbral and Evershed flow structure (Borrero & Ichimoto, 2011).

opposite direction with respect to that displayed by the typical Evershed flow at some azimuths. Figure 2.10 shows the continuum intensity and the LOS velocity evolution in the AR NOAA 11024 studied by Schlichenmaier et al. (2012), where the opposite Evershed flow is visible.

## 2.3 Penumbra formation

---

The presence of the penumbra distinguishes a mature sunspot from a pore. However, how and why the penumbra forms are still unknown, because their study requires long time series observations (several hours) carried out with high temporal, spatial, and

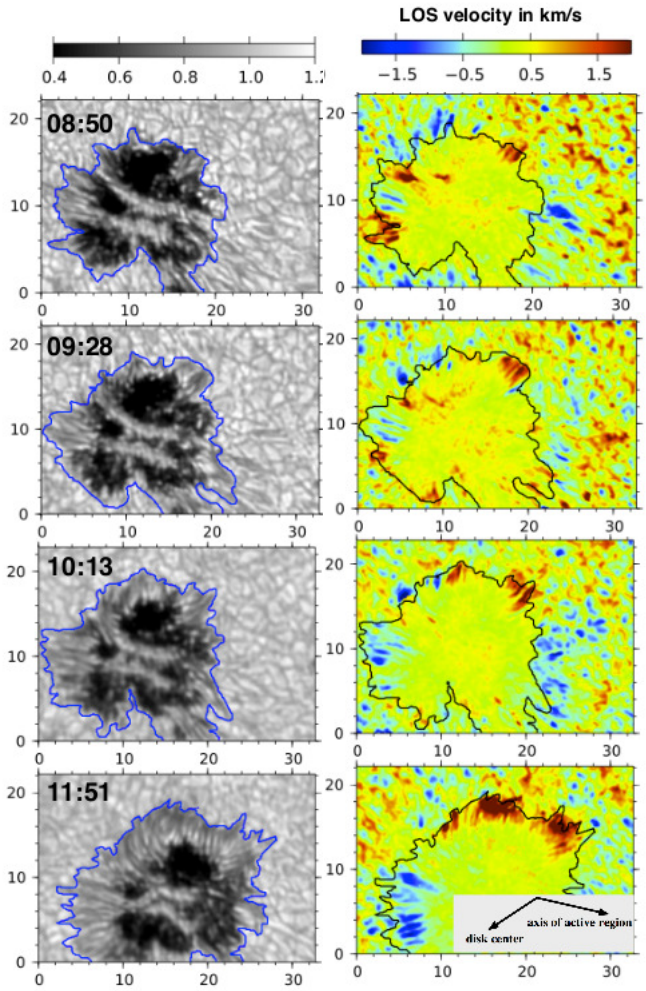


Figure 2.10: Continuum intensity and LOS velocity maps of AR NOAA 11024 (Schlichenmaier et al., 2012)

spectral resolution (Thomas & Weiss, 2004).

Some recent studies have indeed provided some advancements in our knowledge of the formation of the penumbra. For instance, some authors assessed the presence of a critical value of some physical parameters above which penumbra formation takes place. Leka & Skumanich (1998) found that the magnetic field strength in a pore intensifies before penumbra starts to form. They estimated that the initial magnetic flux in a pore is around $2 \times 10^{19}$ Mx, founding a threshold of 1-1.5 $\times$ $10^{20}$Mx, above which the pore can develop a penumbra. From the analysis of spectropolarimetric data taken at the German Vacuum Tower Telescope (VTT), Rezaei et al. (2012) studied the formation of a sunspot penumbra in AR NOAA 11024. They found a magnetic field of the order of kilo-Gauss, inclined of 45° - 60° and extending beyond the edges of the pore (as determined from intensity values). When the penumbra develops, the magnetic boundaries of the spot coincide well with the intensity contours of the pore. They found a critical magnetic field strength $B_{crit} \leq 1.6$ kG and a critical inclination angle of the magnetic field $\gamma \geq 60°$ with respect to the normal to the photosphere, above which the penumbra begins to form.

In this context, Jurcak (2011) investigated nine stable sunspots using Hinode data and concluded that the umbra-penumbra (UP) boundary, traditionally defined by an intensity threshold, is also characterized by a critical value of the vertical component of the

magnetic field, $B_{ver}^{stable} = 1860$ ($\pm$190) G. Jurcak et al. (2015) confirmed this result and found that, during the penumbra formation, the UP boundary migrates toward the umbra and $B_{ver}$ increases. To explain this critical value of $B_{ver}$, they propose that there are two modes of magneto-convection. The penumbral mode takes over in regions with $B_{ver} < B_{ver}^{stable}$, while the umbral mode prevails in regions with $B_{ver} > B_{ver}^{stable}$.

In 2010 Schlichenmaier et al. acquired at the German VTT a 4.40 hr time series of continuum images of the Active Region NOAA 11024. They found that the penumbra formation occurs in sectors in the area away from the opposite polarity, and an individual penumbral sector forms on a time scale of about 30 minutes. In those areas, they found that filaments increase their radial extension, from $1''$ to $5''$ , becoming larger and more numerous. The filaments on the side facing the opposite polarity appeared to be not stable. This region was characterized by elongated granules that appeared and disappeared continuously. These elongated structures were associated with flux emergence and were also found in numerical simulations of Cheung et al. (2008) and Tortosa-Andreu & Moreno-Insertis (2009). These authors concluded that a stable penumbra cannot form in the region of flux emergence, because the strong dynamics owed to ongoing flux emergence prevent the settlement of the penumbral field.

Recently, Lim et al. (2013) found that penumbral filaments

were formed in a region on the side toward the opposite polarity of an AR. In this region a series of elongated granules were detected in association with an emerging flux region. However, they detected also cases where the flux emergence, even if accompanied by a series of elongated granules, did not form the penumbra. They explained this double behavior with the presence or absence of strong overlying canopy fields, concluding that both the amount of emerging flux and the existence of strong canopy field are important in the penumbra formation.

There are two main explanations for penumbra formation. Leka & Skumanich (1998) suggested that emerging, horizontal field lines could be trapped and form a penumbra rather than continuing to rise to higher layers, due to the presence of the overlying magnetic canopy in the emerging region.

In contrast, Shimizu et al. (2012) and Romano et al. (2013, 2014) suggested that the field lines of the magnetic canopy, already existing at a higher level of the solar atmosphere and overlying the pore, may be responsible for the formation of the penumbra if they sink down into the photosphere and below the solar surface (see sketches in Figures 2.11 and 2.12). In fact, they revealed some signatures of penumbra formation around pores in the chromosphere, that appeared earlier than in the photosphere. Shimizu et al. (2012), using images in the Ca II H 396.8 nm line acquired with the Hinode Solar Optical Telescope, showed that in AR NOAA 11039 a 3″- 5″ wide annular zone surrounding a

pore appeared soon after the pore formation and was seen for about 10 hrs until the penumbra formation.

Using spectro-polarimetric data, Romano et al. (2013, 2014) detected the presence of several patches at the edge of the annular zone around a pore of the AR NOAA 11490 in photophere, with a typical size of about 1″. Those patches were characterized by a rather vertical magnetic field with polarity opposite to that of the pore. Those patches showed radially outward displacements with horizontal velocities of about 2 km $s^{-1}$, that have been interpreted as due to portions of the pore's magnetic field returning beneath the photosphere, being progressively stretched and pushed down by the overlying magnetic fields (see the sketch in Figure 2.12).

A last aspect that needs to be considered in this context was reported by Kitai et al. (2014). Their study concerns the different observed ways to form the penumbra. They observationally and morphologically studied and classified the penumbra formation in NOAA 10978 using G-band images acquired by SOT/Hinode.

In particular, they found three paths to penumbral formation:

- **active accumulation of magnetic flux**: the magnetic flux concentrations move to form a denser magnetic concentration.

- **rapid emergence of magnetic fields**: new magnetic flux of the same polarity of the protospot emerges.

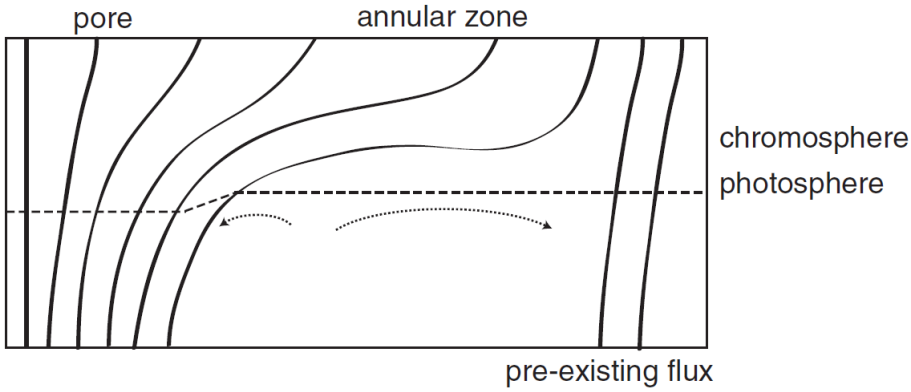


Figure 2.11: Sketch of magnetic field configuration before the penumbral formation. The nearly horizontal dashed line indicates the photospheric ($\tau$=1) level. The dotted lines with the arrow head are large-scale gas flows in the subsurface layer (Shimizu et al., 2012).

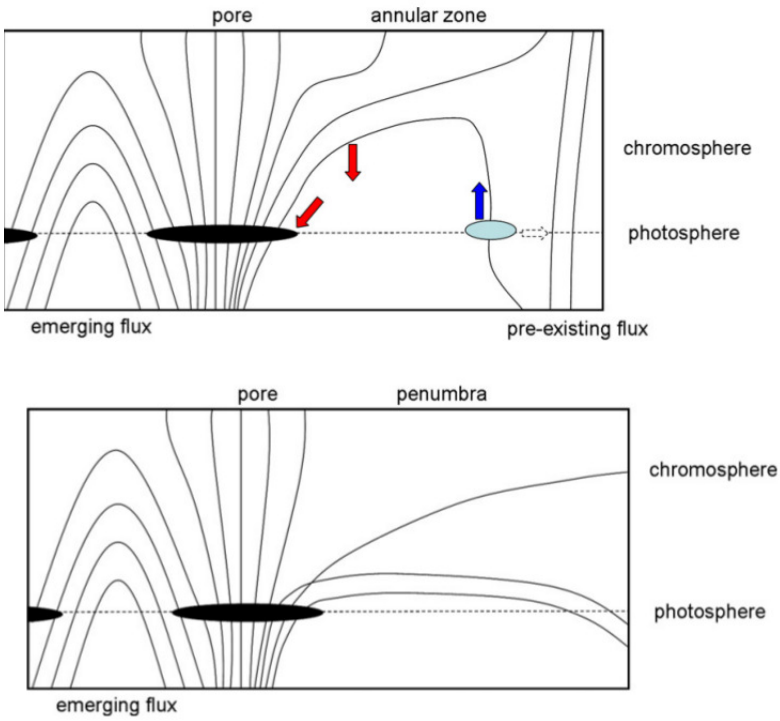


Figure 2.12: Sketch of magnetic field configuration before (upper panel) and after (bottom panel) the penumbra formation. The colored arrows indicate the prevalent motions observed at photospheric and chromospheric levels, while the dashed arrow indicates the radially outward displacement of the patches (blue oval). (Romano et al., 2014).

- **appearance of twisted or rotating magnetic flux tubes**: the penumbra filaments are seen rotating with respect to the radial direction from the umbra centre.

In their work, they also classified the AR 11024 studied by Schlichenmaier et al. (2010) and the AR 11490 studied by Romano et al. (2013, 2014) and Murabito et al. (2016, 2017) as cases of active accumulation of magnetic flux.

Their findings need to be better investigated with spectropolarimetric observations.

## 2.4 Simulations of penumbra formation

Noticeable progress in sunspot modeling using realistic MHD simulations has been reached in the last 10 years. We recall however that developing radiative MHD simulations of sunspots with sufficient resolution to obtain good information on the magneto-convection energy transport requires large computational domain and computing power.

Recent simulations of umbra/penumbra transition have been developed including regions of granulation and increasing the computational domain with respect to previous MHD simulations of a sunspot umbra performed by Schüssler & Vögler (2006). To minimize the computational expenses, it is useful to model the sunspots in 'slab' geometry, i.e. considering a small rectangular section of a sunspot. The first realistic MHD simulation following this scheme was performed by Heinemann et al. (2007). The main result of this simulation is the formation of a filamentary structure in the outer part of the sunspot. However the penumbra filaments of this simulation were shorter than those observed. With the same configuration, but changing the extension of the domain, Rempel et al. (2009a) found penumbra filaments that reach 3 Mm. Recently, Rempel et al. (2009b) performed a simulation of a pair of opposite polarity big sunspots

(35 Mm) in order to cover a variety of combinations of field strength and inclination angle in a single simulation run (Rempel & Schlichenmaier, 2011). The sunspots evolved for 3.6 hours during the simulation, sufficient to study the penumbral structure and the dynamics. Both spots have an identical magnetic flux ($1.6 \times 10^{22}$ Mx), while they have a different central field strength of about 3 kG and 4 kG, respectively. As a consequence, the weaker spot shows more umbral dots and a most extended penumbra is found in the x-direction. For the first time, they found an extended outer penumbra with a strong radial outflow (up to 5 $\mathrm{km\,s^{-1}}$). The onset of this strong outflow is related to the magnetic field inclination. The outflow velocity increases and the field becomes more inclined at great distance from the umbra. In the inner part of the simulated penumbra the magnetic field inclination varies from 40° to 90°, while in the outer part the highly inclined fields dominate. Although their simulation is realistic, it does not accurately reproduce all aspects of the observed penumbral filaments (Rempel et al., 2009b).

Taking into account that it is not easy to investigate the process of sunspot formation and decay within a single simulation, usually the processes in lower and upper convective zone are modelled separately.

Recently, Chen et al. (2017) presented a numerical model of sunspot and active region formation through the emergence of flux bundles generated in a solar convective dynamo. Their

simulations are based on the method shown in Cheung et al. (2010) and Rempel & Cheung (2014). Concerning the penumbra formation, the main results presented by Chen et al. (2017) are:

1. In previous MHD simulations the penumbra filaments were obtained forcing the strong horizontal magnetic field around the umbra using a special configuration as in Rempel et al. (2009b) or using the top boundary as in Rempel (2012). In this simulation, penumbral structures form spontaneously, without any artificially enforced field inclination, and with a length similar to the observed ones.

2. The long penumbral filaments are more likely to appear in regions with ongoing flux emergence. On the side away from the opposite polarity the filaments are less and shorter.

3. Even if part of the penumbra shows an outflow consistent with the Evershed effect, the penumbra filaments are dominated by radial inflows. These filaments tend to appear at the inner side of active regions, where the flux emergence is more active. This inflow coud be related to the emerging magnetic flux.

# Chapter 3

# High resolution observations

The physical processes occurring during the AR evolution produce an abundant variety of structures on different spatial and temporal scales and many aspects need to be investigated with high spatial, spectral and temporal resolution. As previously described, these processes are due to the interaction between the plasma and the magnetic field, from the convective zone to the upper atmopheric layers. The main questions are how the magnetic field rises into different atmopheric layers and how behaves due to the interaction with the plasma. For this reason, it is necessary to use the spectropolarimetric data that allow us to infer all the magnetic field vector components and therefore to follow the AR magnetic evolution.

In this thesis I used spectropolarimetric data acquired by the

Interferometric BIdimensional Spectropolarimeter (Cavallini, 2006) mounted at Dunn Solar telescope. I also analyzed data acquired by the Solar Dynamic Observatory(SDO)/Helioseismic Magnetic Imager(HMI) instrument.

## 3.1 Ground-based observations: Interferometric BIdimensional Spectropolarimeter/DST

---

One of the solar telescopes characterized by the higher resolution is the Dunn Solar Telescope (DST), located in Sacramento Peak, New Mexico. Its tower is high 41.5 m and deep 67 m. Since June 2003 at the exit of the high-order Adaptive Optic (OA) is mounted the interfometer IBIS, built by the INAF-Arcetri Astrophysical Observatory, with the support of the Department of Physics and Astronomy of the University of Florence, and the Department of Physics of the University of Rome - Tor Vergata. IBIS is composed by two Fabry-Perot interferometers (FPI) used in axial-mode and in classic mount. The IBIS layot is shown in Figure 3.1, where the principal optical path is represented with solid line, while the secondary ones are shown by dashed lines.

At the exit of the AO, a pupil image is formed near the first mirror M1, at the focus of the transfer lens L0. This lens and two other mirrors (M2, M3) form the solar image on the field

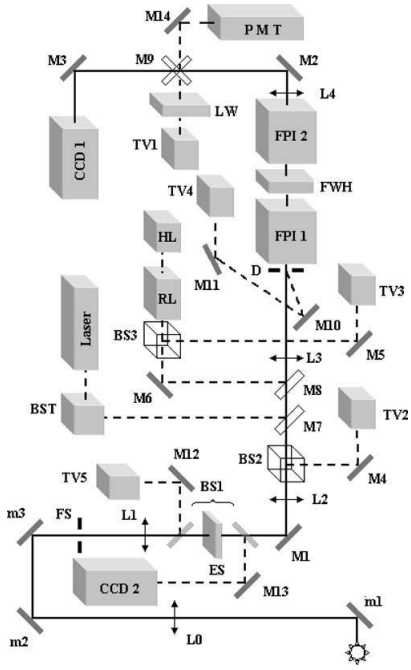


Figure 3.1: IBIS schematic drawing. The meaning of the labels is as follows. BS: beamsplitter; BST: beam steering; CCD: CCD camera; ES: electronic shutter; FPI: Fabry-Perot interferometer; FS: field stop; FWH: filter wheel; HL: halogen lamp; L: lens; LW: lens wheel; M, m: mirror; PMT: photomultiplier; RL: relay lenses; TV: TV camera; W: window. (Cavallini, 2006)

stop (FS) of the instrument. The image is 21.3 mm in diameter, corresponding to 80″on the Sun. Three lenses (L1, L2, L3) and a folding mirror (M1) successively collimate the solar and the pupil image. After L3, there are two FPIs and between them, a filter wheel (FWH) carrying a hole, a dark slide and five interference filters. In the optical path there is a fourth lens (L4) and two further folding mirrors (M2, M3) that form a solar image of 6.85 mm in diameter, on a CCD camera (CCD1). The solar image is inscribed in a square area measuring 1007×1007 pixels on a CCD with 1024×1024 pixels. This implies an image scale of $0.08''\text{pixel}^{-1}$ (Cavallini, 2006).

The main characteristics of IBIS are reported in Table 1.1

Table 3.1: IBIS characteristics (Cavallini, 2006)

| | |
|---|---|
| Spectral Range | 580-860 nm |
| Spectral resolving power | 200000-270000 |
| Field of view (circular) | 80″ |
| Image scale | $0.08''\text{pix}^{-1}$ |
| Exposure time | 32-50 ms |
| Acquisition rate | $\simeq$2.5 frames $\text{s}^{-1}$ |

## 3.2 Space-based observations: SDO

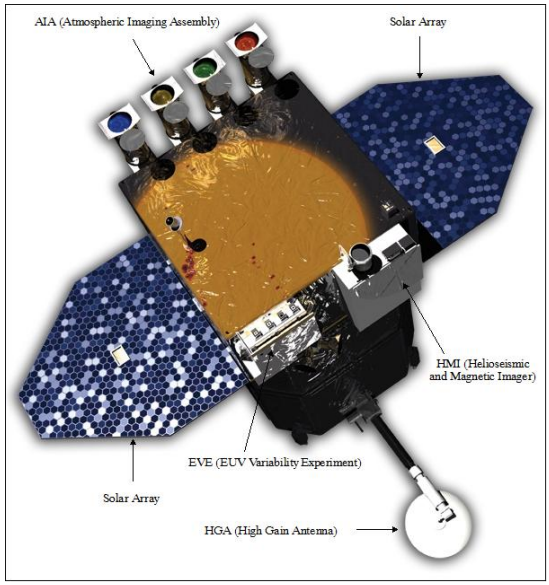


Figure 3.2: SDO and its instruments

In order to investigate the ARs evolution it is useful to combine high spatial, spectral and temporal resolution data taken by ground-based observatories with data taken by space-based telescopes, which guarantee a wide and continous temporal range of observations. For this reason, in this work I also used data taken by the HMI and AIA instruments on board of SDO.

SDO is the first mission of the NASA Program 'Living with

a Star'. The goal is to study the solar variability and its impact on the Earth. The satellite was launched on February 11, 2010 (SDO, Pesnell et al., 2012). It contains three instruments: the *Atmospheric Imaging Assembly* (AIA), the *Extreme Ultraviolet Variability Experiment* (EVE) and the *Helioseismic and Magnetic Imager* (HMI). In particular, the latter instrument allows measurements of the solar magnetic field using the Fe I 617.3 nm absorption line. Figure 3.2 shows a SDO picture and its components.

The HMI instrument is a new version of the Michelson Doppler Imager (MDI) instrument, which was part of the Solar and Heliospheric Observatory (SOHO, Scherrer et al., 1995). Whit respect to MDI, HMI has higher spatial resolution ($0\farcs5$) and temporal resolution (45 seconds) (Pesnell et al., 2012). It is the first space-based instrument to map the full-disk photospheric vector magnetic field with high cadence and continuity.

HMI consists of a refracting telescope, a polarization selector (3 rotating waveplates), an image stabilization system (ISS), 5 element Lyot filter and 2 tunable Michelson interferometers. The combined Lyot-Michelson filter system in HMI produces a transmission profile with a FWHM of 76 mÅ. In addition, there are two 4096×4096 pixel CCD cameras. The twin cameras of HMI operate independently. One is referred to as the 'Doppler camera', where the objective is to measure the line-of-sight (LOS) component of the magnetic field. The second camera is referred

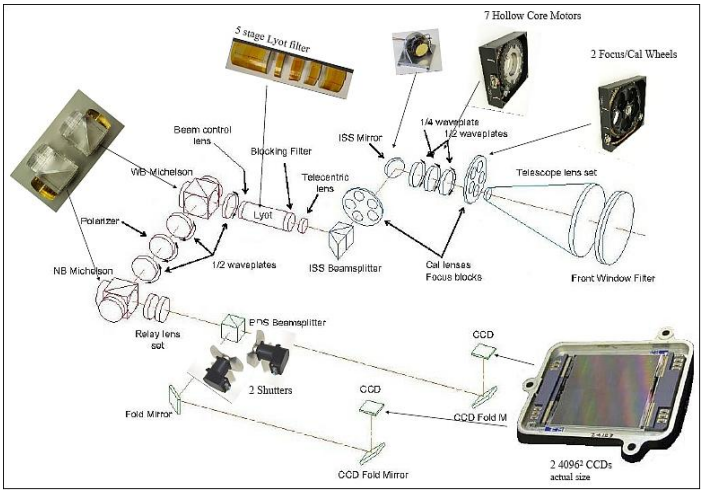


Figure 3.3: HMI optical path diagram

to as 'Magnetic camera' and the objective is to measure the vector magnetic field with a specific polarization sequence.

Figure 3.3 shows the HMI optical scheme: sunlight travels through the instrument from the *Front window filter* to the two CCD cameras. The front window is a filter with a 50Å bandpass that reflects most of the incident sunlight. A refracting telescope, consisting of primary lens and a secondary biconcave lens, with a 14 cm diameter follows the front window. Between the telescope and the polarizing beamsplitter the focus/calibration mechanism, two polarization selection mechanism and the images stabilization system (ISS) tip-tilt mirror are positionated. The filter section contains:

- a telecentric lens
- an 8Å bandpass dielectric blocking filter
- a Lyot filter
- two polarizing Michelson interferometers
- reimaging optics

Following the Lyot filter there is a beam splitter, which feeds two identical shutters and CCD camera assemblies. The telecentric lens at the entrance of the Lyot filter produces a collimated beam for the subsequent filter. This ensures that the angular distribution of light passing through the filters is identical for each image point. At the exit of the Lyot filter, a pair of lenses reimages the primary focus onto the detectors. Finally, a beamsplitter divides the light between the two CCD cameras.

The Space weather HMI AR Patches (SHARPs, Bobra et al., 2014) data are among the data produced by HMI/SDO and give maps in patches, where magnetic field concentrations are tracked automatically. SHARPs data follow each significant patch of solar magnetic field from before its appearance until it disappears. The quantities included in these data are the photopheric magnetic field vector and its uncertainty, the Doppler velocity, the continuum intensity and the LOS magnetic field.

The AIA instrument (Lemen et al., 2012) is designed to study the transition region and the solar corona, taking simultaneous

full disc images in multiple wavelengths (up to half a solar radius above the solar limb), with a resolution of 1.5″ and 12 second temporal cadence or better.

The AIA consists of four Cassegrain telescopes to provide narrow-band imaging of seven extreme ultraviolet (EUV) band passes centered on specific lines (see Table 3.2). One of the telescopes observes the C IV line (near 1600 Å) and the nearby continuum (1700 Å) and has a filter that observes in the visible to enable coalignment with images from other telescopes.

Table 3.2: The primary ions observed by AIA (Lemen et al., 2012).

| **Channel** | **Primary ion(s)** | **Region of atmosphere** |
|---|---|---|
| 4500 Å | continuum | photosphere |
| 1700 Å | continuum | temperature minimum, photosphere |
| 304 Å | He II | chromosphere, transition region |
| 1600 Å | C IV + cont. | transition region, upper photosphere |
| 171 Å | Fe IX | quiet corona, upper transition region |
| 193 Å | Fe XII, XXIV | corona and hot flare plasma |
| 211 Å | Fe XIV | active-region corona |
| 335 Å | Fe XVI | active-region corona |
| 94 Å | Fe XVIII | flaring corona |
| 131 Å | Fe VIII, XXI | transition region, flaring corona |

## 3.3 Spectro-polarimetry and data inversion technique

The determination of the magnetic field is one of the most useful methods to investigate the processes occurring in ARs. During the last century the spectroscopy was the most important tool to study the magnetic field. The Zeeman effect was used to study the spectral line broadening in presence of the magnetic field. Despite the importance of spectroscopy, it could not be used to detect the full magnetic field vector B.

However, with the introduction of polarimetry, the study of the polarization state of the radiation, it has been possible to infer the magnetic field vector. The polarized radiation is described by 4 parameters, called Stokes parameters and indicated by I, Q, U and V.

Considering the radiation as the overlay of plane electromagnetic waves, we can describe an electromagnetic wave using only one between electric and magnetic field vector. Then, the electric field components are described as (Landi Degl'Innocenti, 2008):

$$E_1(t) = \varepsilon_1(t)e^{-i\omega t} = A_1(t)e^{-i[\omega t - \phi_1(t)]} \tag{3.1}$$

$$E_2(t) = \varepsilon_2(t)e^{-i\omega t} = A_2(t)e^{-i[\omega t - \phi_2(t)]} \tag{3.2}$$

Where $\omega$ is the angular frequency of the wave and $\varepsilon_1$, $\varepsilon_2$

are two complex constant that can be expressed by four real constants $A_1$, $A_2$, $\phi_1$, $\phi_2$:

$$\varepsilon_1 = A_1 e^{i\phi_1(t)} \tag{3.3}$$

$$\varepsilon_2 = A_2 e^{i\phi_2(t)} \tag{3.4}$$

The Stokes parameters are defined through the following equations:

$$I = kP_I = k(\left\langle \varepsilon_1^* \varepsilon_1 \right\rangle + \left\langle \varepsilon_2^* \varepsilon_2 \right\rangle) \tag{3.5}$$

$$Q = kP_Q = k(\left\langle \varepsilon_1^* \varepsilon_1 \right\rangle - \left\langle \varepsilon_2^* \varepsilon_2 \right\rangle) \tag{3.6}$$

$$U = kP_U = k(\left\langle \varepsilon_1^* \varepsilon_2 \right\rangle + \left\langle \varepsilon_2^* \varepsilon_1 \right\rangle) \tag{3.7}$$

$$V = kP_V = k(\left\langle \varepsilon_1^* \varepsilon_2 \right\rangle - \left\langle \varepsilon_2^* \varepsilon_1 \right\rangle) \tag{3.8}$$

Where $P_I$, $P_Q$, $P_U$, $P_V$ are parameters of the polarization ellipse and $\varepsilon_1^* \varepsilon_1$ are the components of the polarization tensor.

When we consider the interaction between radiation and matter in stellar and solar atmosphere we need to recall the radiative transfer equation :

$$\mu \frac{dI_\lambda}{d\tau_c} = I_\lambda - \frac{\varepsilon_\lambda}{\kappa_\lambda} = I_\lambda - S_\lambda \tag{3.9}$$

where $\mu = cos\theta$ indicates the heliocentric angle, $I_\lambda$ is the specific intensity of radiation field at a given wavelength $\lambda$, $\tau_c$ is the optical depth, $\varepsilon_\lambda$ and $\kappa_\lambda$ are the emission and absorption coefficients, respectively, and $S_\lambda$ is the source function.

Unno (1956) was the first to derive the radiative transfer equation in the presence of a magnetic field (RTE) by means of classical electrodynamics. Later, Landi Degl'Innocenti (1983) managed to deduce RTE on the basis of more general quantum mechanical principles.

Using Stokes calculus, the RTE in presence of the magnetic field can be written as (Borrero & Ichimoto, 2011):

$$\frac{dI_\lambda(X[\tau_c])}{d\tau_c} = \hat{\kappa}_\lambda(X[\tau_c])[I_\lambda(X[\tau_c]) - S_\lambda(X[\tau_c])] \tag{3.10}$$

where $I_\lambda(X[\tau_c]) = (I, Q, U, V)^\dagger$ is the transpose of the Stokes vector at given wavelength $\lambda$, $\hat{\kappa}_\lambda(X[\tau_c])$ is the propagation matrix at a wavelength $\lambda$ and X represents the physical parameters that describe the solar atmophere:

$$X(\tau_c) = [B(\tau_c), T(\tau_c), P_g(\tau_c), P_e(\tau_c), \rho(\tau_c), V_{los}(\tau_c)] \tag{3.11}$$

where $B(\tau_c)$ is the magnetic field vector, $T(\tau_c)$ is the temperature stratification, $P_g(\tau_c)$ and $P_e(\tau_c)$ are the gas and electron pressure stratification, $\rho(\tau_c)$ is the density stratification and $V_{los}(\tau_c)$ is the stratification with optical depth $(\tau_c)$ of the

LOS velocity. Finally, on the right-hand side of the RTE we have the propagation matrix $\hat{\kappa}_\lambda(X[\tau_c])$ and the souce function $S_\lambda(X[\tau_c])$. The latter is always non-polarized and, therefore, only contributes to Stokes I.

According to Landi Degl'Innocenti & Landi Degl'Innocenti (1985), the formal solution of RTE can be written as (Borrero & Ichimoto, 2011):

$$I_\lambda(X[\tau_c]) = \int_0^\infty \hat{O}_\lambda(X[\tau_c])\hat{\kappa}_{c\lambda}(X[\tau_c])S_\lambda(X[\tau_c])d\tau_c \qquad (3.12)$$

where $\hat{O}_\lambda(0,\tau_c)$ is the evolution operator. If $\hat{O}_\lambda$ is known, it is straightforward to evaluate the RTE. This is the so- called synthesis of Stokes profiles by radiative transfer calculation in an atmosphere of known characteristics. The opposite approach, i.e. inferring $\hat{O}_\lambda$ from a measurement of $I_\lambda = S_\lambda$, is called inversion.

The RTE can be solved analytically and in particular, the SIR (Stokes Inversion based on Response functions) code (Ruiz Cobo & del Toro Iniesta, 1992) solves it.

### 3.3.1 The SIR code

The SIR code is among the inversion techniques that work in syntesis and inversion mode. In the synthesis mode the code solves the RTE for a given atmosphere under some assumptions (defined by X($\tau_c$)) to obtain the Stokes profiles formed in that specified atmosphere.

In the inversion mode, SIR fits any combination of observed Stokes parameters for any arbitrary number of spectral lines. A merit function ($\chi^2$) uses the Levenberg - Marquardt method to minimize the difference between the observed and synthetic Stokes profiles. The expression of the $\chi^2$ is given by:

$$\chi^2 = \frac{1}{4M - L} \sum_{i=1}^{4} \sum_{k=1}^{M} \left[ \frac{I_i^{obs}(\lambda_k) - I_i^{syn}(\lambda_k, X[\tau_c])}{\sigma_{ik}} \right]^2 \quad (3.13)$$

Here $I_i^{obs}(\lambda_k)$ and $I_i^{syn}(\lambda_k)$ represent the observed and synthetic Stokes vector, respectively. The letter L represents the total number of free parameters in X and, thus, the term 4M-L represents the total number of degrees of freedom of the problem (number of data points minus the number of free parameters). The indexes i and k run for the four components of the Stokes vector and for all wavelengths, respectively. Finally, $\sigma_{ik}$ represents the error in the observations ($I_i^{obs}(\lambda_k)$).

### 3.3.2 Azimuth ambiguity

The inversion technique fails when we want to know exactly the direction of the magnetic field. This is called 180°-ambiguity problem in the determination of the azimuth angle of the magnetic field. The expression of the propagation matrix ($\hat{\kappa}_\lambda$) includes 4 terms ($\eta_Q$, $\eta_U$, $\rho_Q$, $\rho_U$) that depend on $2\phi$, where $\phi$ is the azimuthal angle of the magnetic field vector in the plane perpendicular to the observer's LOS (del Toro Iniesta, 2003). These

matrix elements are the same if we take $\phi + \pi$ or $\phi$, therefore, the RTE cannot distinguish the two possibile solutions for the azimuth angle.

There are a lot of techniques developed to solve this problem. Among them, I used the Non Potential Field technique (NPFC) (Georgoulis , 2005). This code assumes that an isolated, current-carrying, solar magnetic structure B is measured on a plane S by means of a longitudinal field $B_l$, a transverse field $B_{tr}$, and an azimuth angle $\phi$ of the transverse field on the LOS reference system. The two ambiguity solutions in this coordinate frame ($[B_l,B_{tr},\phi]$ and $[B_l,B_{tr},\pi+\phi]$) are trasformed to the local, heliographic, reference system to obtain the two solutions. The idea of NPFC code is that the magnetic field vector B can be decomposed into a current-free, vacuum, magnetic field component $B_p$ and a nonpotential, current-currying, magnetic field component $B_c$. This latter is responsible for any electric current J flowing into the magnetic structure via Ampere's law. The code focuses on the vertical electric current density $J_z$ calculated as (Georgoulis , 2005):

$$J_z = \frac{c}{4\pi}(\nabla \times B_c)_z \tag{3.14}$$

# Chapter 4

# Penumbra formation in a region without flux emergence

In this chapter I describe the properties of the plasma, magnetic field and velocity field, during the penumbra formation in a sunspot with no magnetic flux emergence. The data used for this analysis were acquired during an observing campaign at DST, on 28 and 29 May 2012.

## 4.1 Observations

The AR 11490 was observed by IBIS on 28 and 29 May 2012, when it was characterized by a cosine of the heliocentric angle $\mu$=0.95 and $\mu$=0.97, respectively.

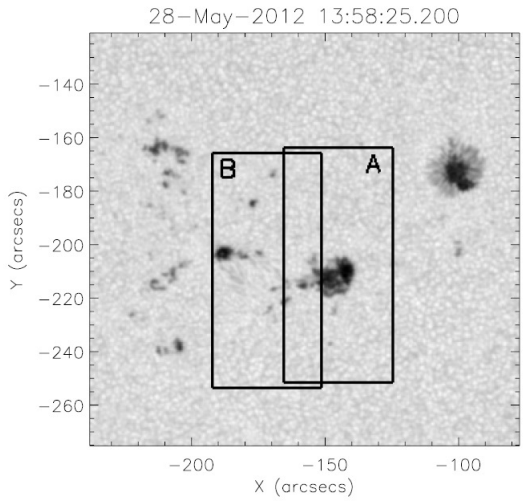


Figure 4.1: Continuum filtergram taken by HMI/SDO at 617.3 nm. The boxes A and B indicate the FOVs observed by IBIS in NOAA AR 11490.

The FOV of IBIS camera, indicated by the boxes A and B in Figure 4.1, is 500 × 1000 pixels, with a pixel scale of 0.″09. The dataset acquired on May 28 consists of 45 scans, 30 concerning the FOV A and 15 the FOV B, through the Fe I 630.25 nm, Fe I 617.30 nm and Ca II 854.2 nm lines. The dataset acquired on May 29 includes 30 scans of the FOV A along the same spectral

lines. Table 4.1 lists the data used for this work.

| *Instrument* | *λ (nm)* | *Time (UT)* | *Field of view* |
|---|---|---|---|
| IBIS/DST | 630.25 | 2012-05-28 13:39-14:12 | FOV A |
| IBIS/DST | 630.25 | 2012-05-29 13:49-14:32 | FOV A |
| SDO/HMI | 617.30 | 2012-05-28 14:58 to 2012-05-29 14:58 | FOV A |

Table 4.1: Details of the data

The Fe I 630.25 nm line was sampled in 30 spectral points with a FWHM of 2 pm, an average wavelength step of 2 pm and an integration time of 60 ms. It was sampled in spectropolarimetric mode. The signal-to-noise ratio of these measurements is about $3 \times 10^{-3}$ in unit of continuum intensity per Stokes parameter.

## 4.2 Analysis

After the standard preliminary reduction, the images were restored using the Multi-Frame Blind Deconvolution (MFBD; Löfdahl, 2002) technique. Then I performed a single-component inversion of the Stokes profiles for all the available scans of the Fe I 630.25 nm line using the SIR code (Ruiz Cobo & del Toro Iniesta, 1992) to determine the magnetic field strength, inclination and azimuth angles. I normalized the spectra to the quiet Sun continuum, $I_c$, and divided the FOV A into three regions,

identified by a different threshold of $I_c$ to take into account different physical conditions of the quiet Sun ($I_c$ >0.9), penumbra (0.7< $I_c$ <0.9) and umbra ($I_c$ <0.7). For the quiet Sun model I used as an initial guess the temperature stratification of the Harvard-Smithsonian Reference Atmophere (HSRA, Gingerich et al., 1971) and a value of 0.1 kms$^{-1}$ for the LOS velocity. In the penumbral model, I changed the initial guess of the temperature (T) and the electron pressure ($p_{e^-}$) according to the penumbral stratification provided by Del Toro Iniesta et al. (1994), and I used an initial value for the magnetic field strength of 1000 G and 1 km s$^{-1}$ for the LOS velocity. Finally, for the umbral model I changed the initial T and $p_{e^-}$ using the values provided by Collados et al. (1994) (an umbral model for a small spot), and I considered an initial value of 2000 G for the magnetic field strength. The temperature stratification of each component was modified with three nodes, although all other quantities were assumed to be height independent. I modelled the stray-light contamination by averaging over all Stokes I spectra the 64 pixels characterized by the lowest polarization degree. A magnetic filling factor was introduced as a free parameter of the inversion, which described the weight being assigned to the local atmosphere relative to the stray-light. The spectral point-spread function of IBIS (Reardon & Cavallini, 2008) was used to take into account the finite spectral resolution of the instrument. Once I obtained the magnetic field strength, the inclination and azimuth angles, I used

the Non-Potential Field Calculation code (Georgoulis , 2005) to solve the 180°-azimuth ambiguity and transform the components of the vector magnetic field into the local solar frame.

In order to measure the LOS plasma velocity, I used a Gaussian fit of the line profiles, i.e., I reconstructed the profiles of the Fe I 630.25 nm line in each spatial pixel by fitting the corresponding Stokes I component with a linear background and a Gaussian shaped line. The values of LOS velocity were deduced from the Doppler shift of the centroid of the line profiles in each spatial point. I estimated the uncertainty affecting the velocity measurements considering the standard deviation of the centroids of the line profiles estimated in all points of the whole FOV. Thus, the estimated relative error in the velocity is $\pm 0.2$ km $s^{-1}$.

The temperature in the umbra is low enough to allow the formation of molecules, blending with the 630.25 nm line. Therefore, all umbral profiles with $I_c < 0.7 I_{qs}$, where $I_{qs}$ is the mean value of the intensity in a region of quiet Sun, were excluded from the calculation of the line shift, and the Doppler velocity in the umbra was set to zero. The reference for the local frame of rest was calibrated by imposing that the plasma in a quiet Sun region has on average a convective blueshift (Dravins et al., 1981) for the Fe I 630.25 line equal to -124 m $s^{-1}$ following Balthasar (1988).

To follow the evolution of the AR I also used and analyzed

SHARP continuum filtergrams, Dopplergrams and the vector magnetograms taken by the HMI on board of Solar Dynamics Observatory (SDO) (Scherrer et al., 2012). These data cover one day of observation, as shown in the table 4.1, with a cadence of 12 minutes. The velocity calibration was the same adpoted for IBIS velocity maps, with a convective blueshift equal to -95 $ms^{-1}$ (Balthasar, 1988).

## 4.3 Results

---

Figure 4.2 shows AR NOAA 11490 at the beginning of the observations, at 13:58 UT on May 28. The positive pore in the dashed box (FOV A in Figure 4.1), forms its penumbra in the following 24 hrs. During the evolution, the pore changes its initial shape, the penumbra starts to form initially on the northern and southern part of the pore; later it develops in the western part and only many hours later it appears in the part toward the opposite polarity (see the left column of Figure 4.5).

The continuum intensity, the magnetic field strength, and the inclination angle maps obtained using the SIR code are shown in Figures 4.3 and 4.4. In particular, the left panels show the maps before the formation of the penumbra on 28 May at 14:00 UT, while the right panels show the sunspot after the penumbra formation on 29 May at 14:31 UT.

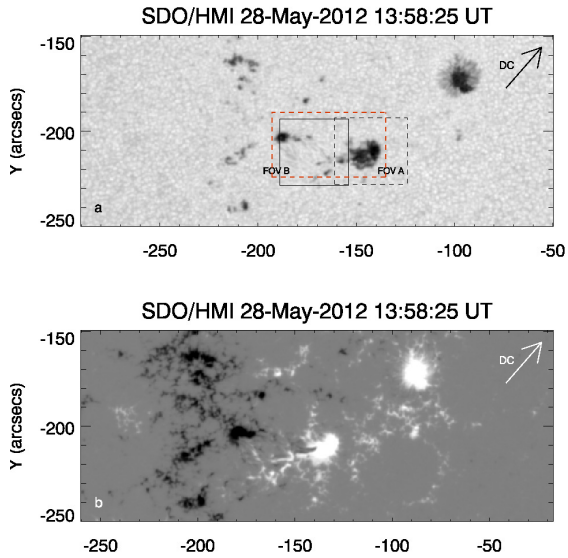


Figure 4.2: Continuum filtegram and LOS magntogram taken by SDO/HMI. The black dashed and continuum boxes in the panel (a) indicate the IBIS FOV's containing the leading and the following spots, respectively. The red box indicates the FOV described in the next chapter 5. Here and in the following figures, north is at the top, and west is to the rigth.The axes give the distance from solar disc center. The arrow points to the disc center.

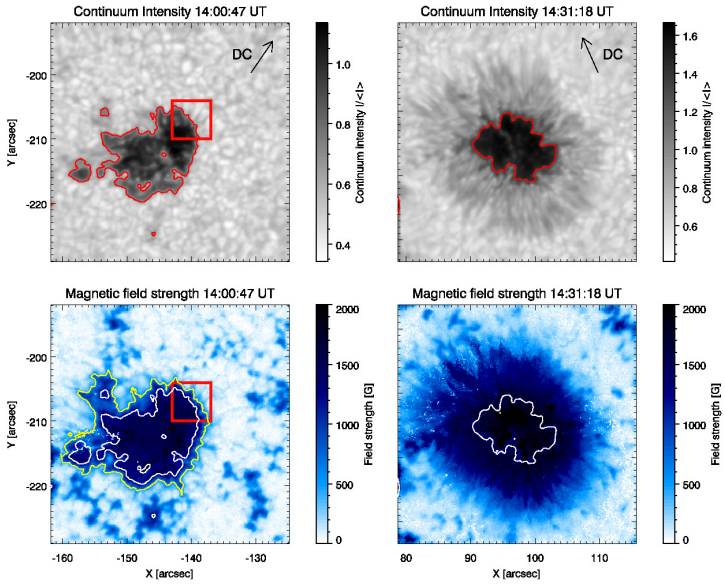


Figure 4.3: Maps of intensity and magnetic field strength on 28 May at 14:00 UT (left, before penumbra formation) and on 29 May at 14:31 UT (rigth, after penumbra formation). The red contour indicates the edge of the pore and of the umbra as seen in the continuum intensity images. In the left panel of the second row, the contours indicate the edge of the pore as seen in the continuum image (white contour) and the annular zone as seen in the magnetic field image (yellow contour), respectively.

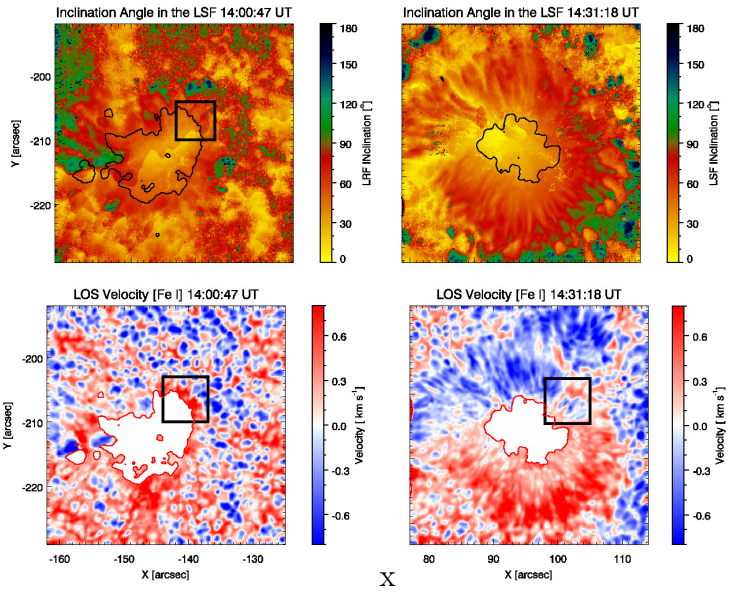


Figure 4.4: Top panels: maps of inclination angle of the magnetic field on 28 May at 14:00 UT (left, before penumbra formation) and on 29 May at 14:31 UT (rigth, after penumbra formation). The black contours indicate the edge of the pore and of the umbra as seen in the continuum intensity images. Bottom panels: LOS velocity maps on 28 and 29 May. The saturation level chosen is $\pm 0.8 \mathrm{kms}^{-1}$. Downflow and upflow correspond to positive and negative velocities, respectively.

Initially the pore is characterized by a magnetic field strength of 1.5 kG. During this stage it is possible to note an annular zone around the pore, where the magnetic field strength is between 500 G and 1000 G (shown by the yellocally variable in space and follows what has been defined as *upside down ballerina skirt structure* of the magnetic field. In fact, I find different sectors with different values of inclination angle of the magnetic field. Moreover, at $\sim 3''$- $4''$ from the edge of the pore in some sectors of the annular zone one can note patches, characterized by an inclination of about 180°, corresponding to the polarity opposite with respect to that of the sunspot (see top panels in Figure 4.4).

At 14:31 UT on May 29, the penumbra is characterized by a magnetic field strength that gradually decreases from about 1.5 kG at the edge of the umbra to about 500 G at the external border of the penumbra (see Figure 4.3, right panel, second row). In the inner penumbra the inclination of the magnetic field is on average 40°-50° and it increases gradually to about 80°-90° at the outer boundary of the penumbra (see top, right panel of Figure 4.4).

Concerning the LOS velocity, downflows larger than 1 $\mathrm{kms}^{-1}$ (Figure 4.4, left bottom panel) are visible in the inner part of the annular zone. It is possible to note that the north-westernn part of the annular zone, is characterized by elongated "cells" in photophere and an inomogeneous field strength (marked by red squares in the left panels of 4.3). The LOS velocity pattern,

when the penumbra was already formed, shows the classic Evershed flow, characterized by flow toward the observer of about -0.5 km $s^{-1}$ in the northeastern part of the penumbra and by flow away from the observer of about 0.6-0.7 km $s^{-1}$ in the southwestern part.

To further study the sunspot evolution, SDO/HMI data have been used. Figure 4.5 shows the evolution of the continuum intensity (first column), LOS velocity (second column), strength and inclination angle of the magnetic field (third and fourth column), from May 28 at 13:58 UT to May 29 at 14:58 UT. Concerning the inclination maps, it is possible to see the same configuration of the magnetic field seen with IBIS. In particular, I identify three sectors characterized by different values of inclination (see the arrows in the top right panel of Figure 4.5). The sector of the annular zone indicated by label 1 (top right panel of Figure 4.5) is characterized by an inclination angle between 90° and 110°. Instead, in the regions labelled as 2 and 3, the inclination is between 30° and 60°. At 14:58 UT on 29 May, when a complete and fully penumbra has developed, the region 1 is characterized by horizontal field in the outer part of the penumbra and by a magnetic field with an inclination of 60°-80° in its inner part. Moreover, from the inclination maps, I note that at the beginning of the observations there are some small magnetic patches surrounding the pore with polarity opposite to the pore. More and more of these features appear with time, forming a

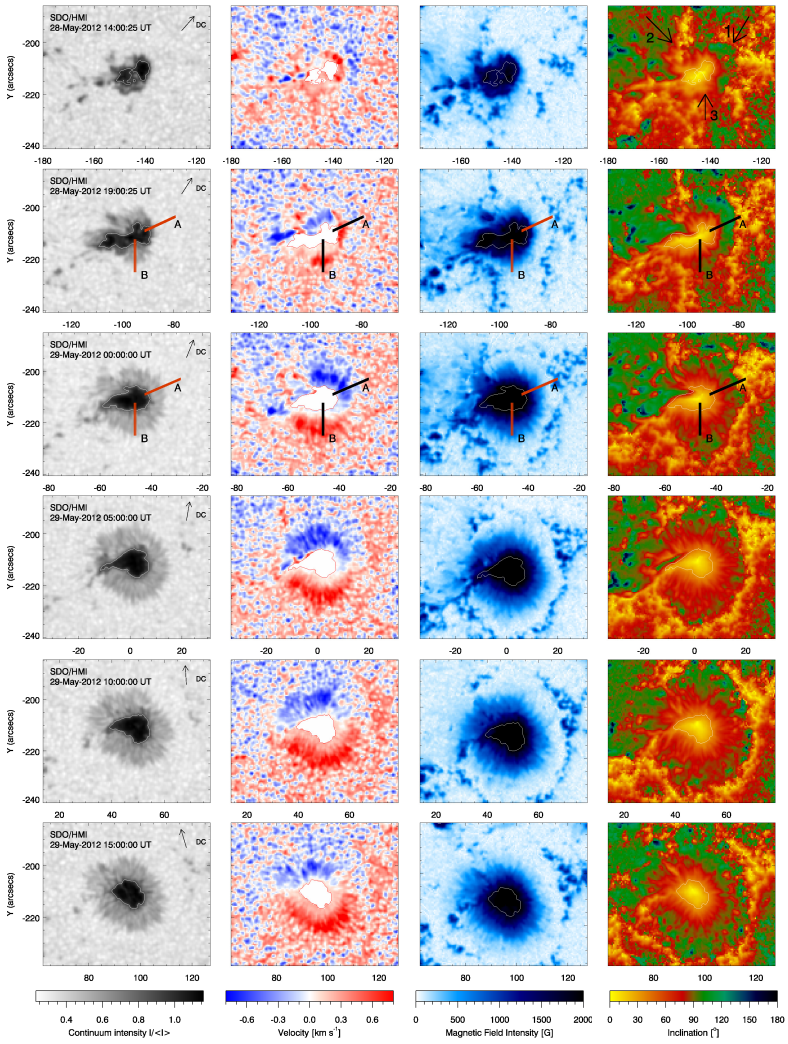


Figure 4.5: From left to rigth: maps of the intensity, LOS velocity, magnetic field strength and inclination angle at different times from 2012 May 28 at 14:58 UT (top row), to 2012 May 29 at 14:58 UT (bottom row) as deduced by SDO/HMI data acquired at 617.3 nm. The yellow contour in the inclination map indicates the edge of the pore or umbra as seen in the continuum intensity image. Positive and negative velocities correspond to downflows and upflows, respectively. The arrows in the first inclination map indicate the sectors described in the text. The 2 pixel wide segment A in each image of the second and third row is used for the analysis shown in Figures 4.8 and 4.9

ring around the sunspot. This ring moves away from the spot with time, presumably driven by the moat flow.

The second column of Figure 4.5 shows the evolution of the LOS velocity. Before the formation of the penumbra, on May 28, like in IBIS observations, in the north-western part of the pore there is a significant redshift corresponding to velocities around 0.4-0.6 $\mathrm{km\,s^{-1}}$, opposite to that of the expected Evershed flow. The sequence of the LOS velocity maps shows that, while the penumbra is forming, the velocity pattern changes and a flow of opposite sign appears, in agreement with the Evershed flow.

To better understand the onset of the Evershed flow I analyzed the evolution of the continuum intensity, LOS velocity, inclination and strength of the magnetic field in the 2 pixel wide and 25 pixels long segment A, overplotted in the second row of Figure 4.5 and in all frames of Figure 4.6. From 21:12 UT to 21:58 UT on 28 May (Figure 4.6) we see that the selected segment lies in a sector where the penumbra is forming. The blushifted region covers a larger and larger range of azimuths around the spot (top rigth panel of Figure 4.6) and the redshifted area decreases with time. Figure 4.7 shows the evolution of the continuum intensity and the LOS velocity along the segment A from 19:00 UT to 24:00 UT on 28 May. The positions of the umbra-quiet Sun boundary before the penumbra formation and the UP boundary after the penumbra formation are calculated computing the maxima in the derivative of the continuum

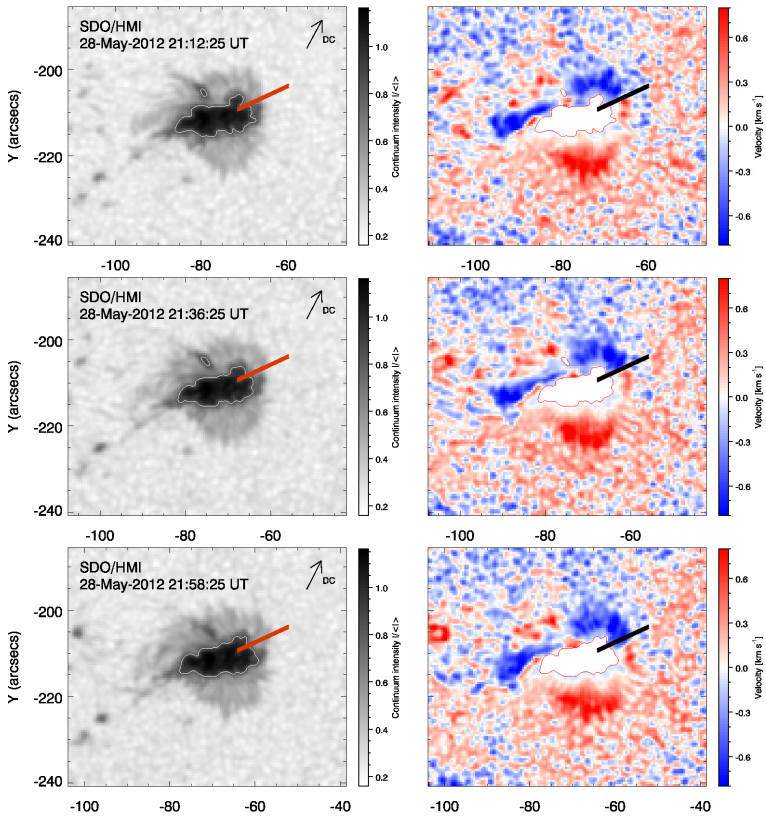


Figure 4.6: Maps of the continuum intensity and LOS velocity from 2012 May 28 at 21:12 UT to 2012 May 28 at 21:58 UT.

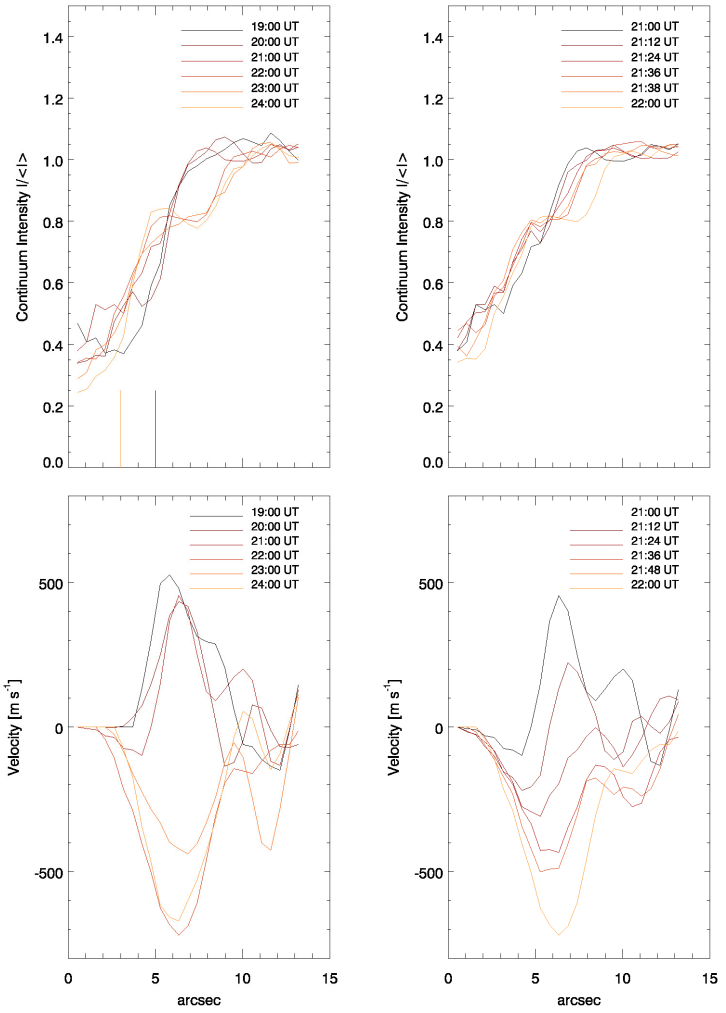


Figure 4.7: Variation of the continuum intensity (top panels) and of the LOS velocity (bottom panels) along the segment A. The origin of the horizontal axis denotes the end of the segment within the umbra. The left and the rigth panels cover interval of 5 hr and 1 hr, respectively. In the top left panel we report the position of the umbra-quiet Sun boundary at 19:00 UT and the position of the umbra-penumbra (UP) boundary at 24:00 UT using vertical bars at coordinates 3″and 5″, respectively.

intensity signal along the selected segment. I display them in the top left panel of Figure 4.7 with black and orange vertical bars, respectively. Following the LOS velocity evolution (bottom left panel of Figure 4.7) it is clear the transition from redshift (see the curves taken at 19:00, 20:00 and 21:00 UT) to blueshift (see the curves taken at 22:00, 23:00 and 24:00 UT). The maximum of the upflow velocity is reached at 22:00 UT and it is 700 $\mathrm{m\,s^{-1}}$. In the bottom rigth panel of Figure 4.7, it is shown in more detail the transition from redshift to blueshift occurring between 21:00 and 22:00 UT on May 28.

Concerning the magnetic field, its evolution along the segment A is shown in Figure 4.8. It is possible to note that, between 6″ and 13″ from the inner edge of the segment, the magnetic field strength (Figure 4.8, bottom panels) changes significantly (about 400 G). The inclination angle in the region between 3″and 7″.5 reaches values up to 80°, indicating positive polarity. In particular, at 7″.5, corresponding to the outer edge of the penumbra, the inclination angle varies from 80° to 70°, becoming more vertical. In the region between 8″and 13″, beyond the outer penumbral boundary, the magnetic field changes sign. At 19:00 UT the inclination is larger than 90° but at 24:00 UT is smaller than 90°. This area does not correspond with the penumbra, but is linked with the moat region. Surprinsingly, the magnetic field strength increases only some minutes after the Evershed-like flow had already established.

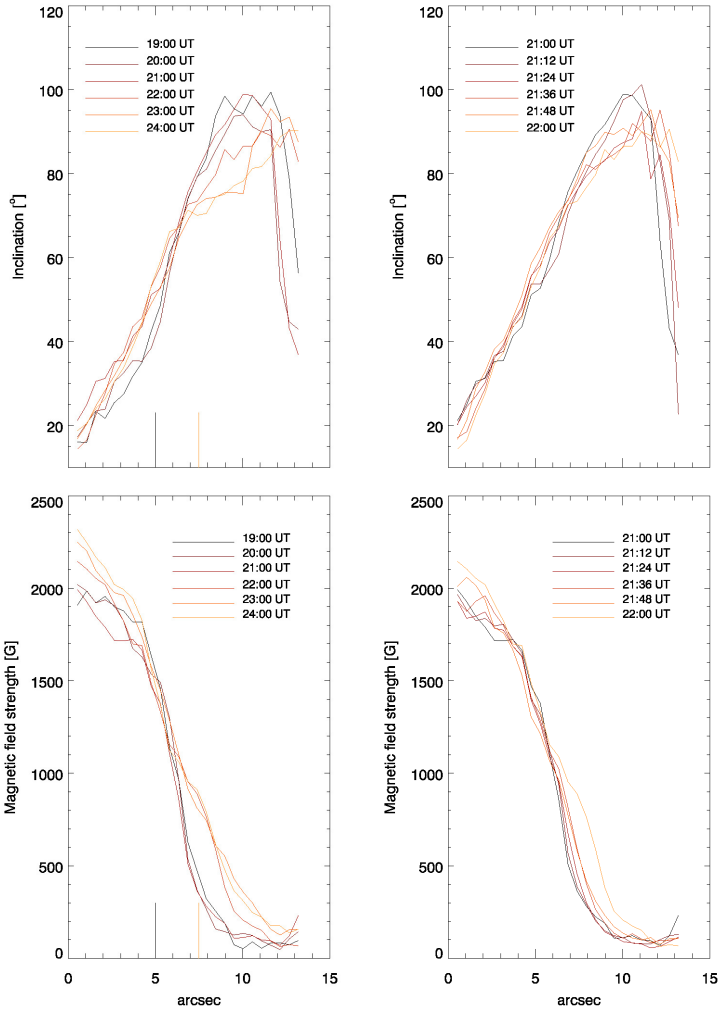


Figure 4.8: Variation of inclination angle (top panels) and strength of the magnetic field (bottom panels) along the segment A. The origin of the horizontal axis denotes the end of the segment within the umbra. The left and the rigth panels cover interval of 5 hr and 1 hr, respectively. In the top left panel we report the position of the umbra-quiet Sun boundary at 19:00 UT and the position of the umbra-penumbra (UP) boundary at 24:00 UT using vertical bars at coordinates 3″and 5″, respectively.

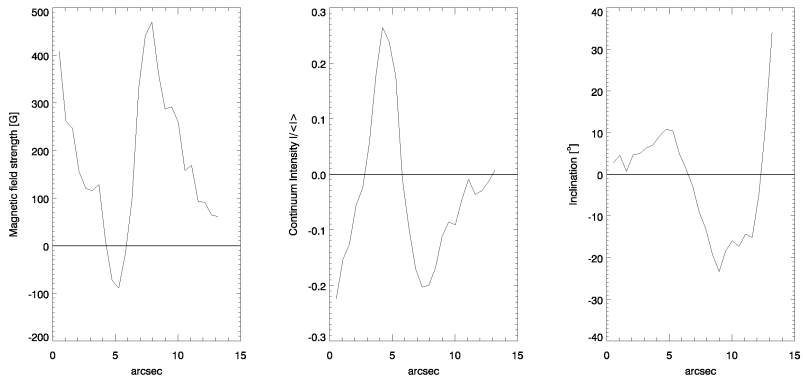


Figure 4.9: Differences between the continuum intensity, magnetic field strength and inclination angles measured at 24:00 UT on 28 May and at 19:00 UT.

Figure 4.9 reports the differences between the values of the continuum intensity, magnetic field strength and inclination angle calculated on May 28 at 24:00 UT and at 19:00 UT. The left panel of Figure 4.9 shows that the continuum intensity decreases by about 20 % of the quiet Sun value in about 5 hrs between 6″ and 11″ from the inner edge of the segment and it increases by about 27 % between 2″ and 6″ . Between 6″ and 9″ from the inner edge of the segment the magnetic field increases by about 500 G in 5 hrs (middle panel of Figure 4.9). The decrease of the magnetic field, between 4″ and 6″ , together with the increase of the continuum intensity, can be attributed to the shrinking of the pore field and to the consequent inward migration of the UP boundary Jurcak (2011). The right panel of Figure 4.9 shows a

variation in the inclination angle of the magnetic field up to 20° and the vertical component of the field changes sign.

Another segment, B, is drawn in the second row of Figure 4.5 and the same analysis like that for the segment A was performed. The segment B lies in a sector where the penumbra forms a few hours before the sector analyzed above, and the onset of the Evershed flow occurs in about 3 hrs, from 15:00 UT to 19:00 UT.

# Chapter 5

# Penumbra formation in a region of flux emergence

This chapter reports the study of the formation of the penumbra in a region of flux emergence. The region under analysis is the following part of AR 11490, located in the FOV B indicated by the solid box in the continuum map of Figure 4.2.

## 5.1 Observations and Analysis

To perform this part of my work I used photospheric and chromospheric data acquired by IBIS and, to study the entire evolution of the active region, I also used HMI/SDO photospheric data, reported in Table 5.1.

Concerning the IBIS dataset, the instrument characteristics

| *Instrument* | $\lambda$ *(nm)* | *Time (UT)* | *Field of view* |
|---|---|---|---|
| IBIS/DST | 617.30 | 2012-05-28 13:39-14:12 | FOV A |
| IBIS/DST | 617.30 | 2012-05-28 14:19-14:38 | FOV B |
| IBIS/DST | 854.20 | 2012-05-28 14:19-14:38 | FOV B |
| IBIS/DST | 617.30 | 2012-05-29 13:49-14:32 | FOV A |
| SDO/HMI | 617.30 | 2012-05-28 13:58 to 2012-05-29 20:58 | Full FOV |

Table 5.1: Data used to study the formation of the penumbra in the following sunspot of AR 11490

are the same described in the Chapter 4 and in Murabito et al. (2016). In particular, as already mentioned, the AR 11490 was observed on May 28, along the Fe I 617.30 nm, Fe I 630.25 nm and Ca II 854.2 nm lines.

The photospheric spectral line Fe I 617.30 nm was sampled with a spectral profile having a FWHM of 2 pm, an average wavelength step of 2 pm and an integration time of 60 ms. It was sampled in spectropolarimetric mode with 24 spectral points. The Ca II 854.2 nm line was sampled in spectroscopic mode with 25 spectral points.

I applied the same calibration described in Chapter 4. The magnetic field strength, inclination and azimuth angles were retrieved performing a single-component inversion of the Stokes profiles for all the available scans of the Fe I 617.30 nm line using the SIR code (Ruiz Cobo & del Toro Iniesta, 1992), using the same initial models already mentioned in Chapter 4.

IBIS and SDO/HMI images were co-aligned, taking into ac-

count the different pixel sizes, using as a reference the first spectral image in the continuum of the Fe I 617.3 nm line taken by IBIS at 14:30 UT on 2012 May 28 and the continuum filtergram closest in time taken by SDO/HMI.

Maps of the mean circular polarization averaged over the line, $V_s$, and of the mean linear polarization signal, $L_s$, were calculated using

$$V_s = \frac{1}{12\,\langle I_c \rangle} \sum_{i=6}^{17} \epsilon_i \, |V_i| \tag{5.1}$$

$$L_s = \frac{1}{12\,\langle I_c \rangle} \sum_{i=6}^{17} \sqrt{Q_i^2 + U_i^2} \tag{5.2}$$

where $\langle I_c \rangle$ is the continuum intensity averaged over the IBIS FoV, $\epsilon = 1$ for the first 6 positions, and $\epsilon = -1$ for the other 6 positions, in the blue and red wings of the line, respectively, and $i$ runs from the $6^{\text{th}}$ to the $17^{\text{th}}$ wavelength positions.

## 5.2 Results

---

The formation of the first penumbral sector in the following part of AR 11490 occurred on May 28, 2012, between 15:00 UT and 20:00 UT, as shown in the area indicated by the red box in Figure 5.1. The area of the umbra expands from 15:00 UT to 18:00 UT as a result of the merging between the following pore and a patch of the same polarity (see the green arrow in

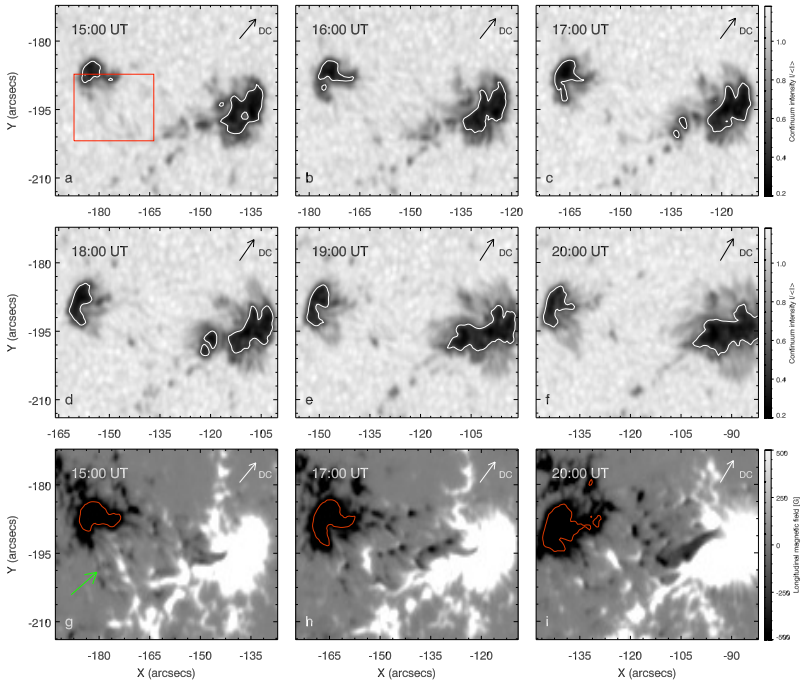


Figure 5.1: (a)-(f) Continuum filtegrams taken by SDO/HMI on May 28 at the time given at the top of each panel, showing the evolution of AR NOAA 11490. White contours in the continuum images indicate the edge of the pore ($I_c = 0.5$). The red box in (a) indicates the sub-FOV displayed in Figure 5.2. (g)-(h) LOS magnetograms taken by SDO/HMI. The values are saturated at $\pm$500 G. Red contours in the magnetograms indicate the area characterized by negative magnetic flux density of about -900 G. The green arrow indicate a patch of the same polarity as the following pore.

Figure 5.1(g)). In this respect, the area of the umbra, determined by contours with a threshold of $I_c = 0.5$, increases by about 42.5 arcsec$^2$ in 5 hrs (from about 35 arcsec$^2$ at 15:00 UT to 77 arcsec$^2$ at 20:00 UT) (Figures 5.1(a)-(f)). In the same way, the area characterized by negative magnetic flux grows by about 60 arcsec$^2$, as derived by contours at -900 G in the magnetograms shown in Figure 5.1(g)-(i).

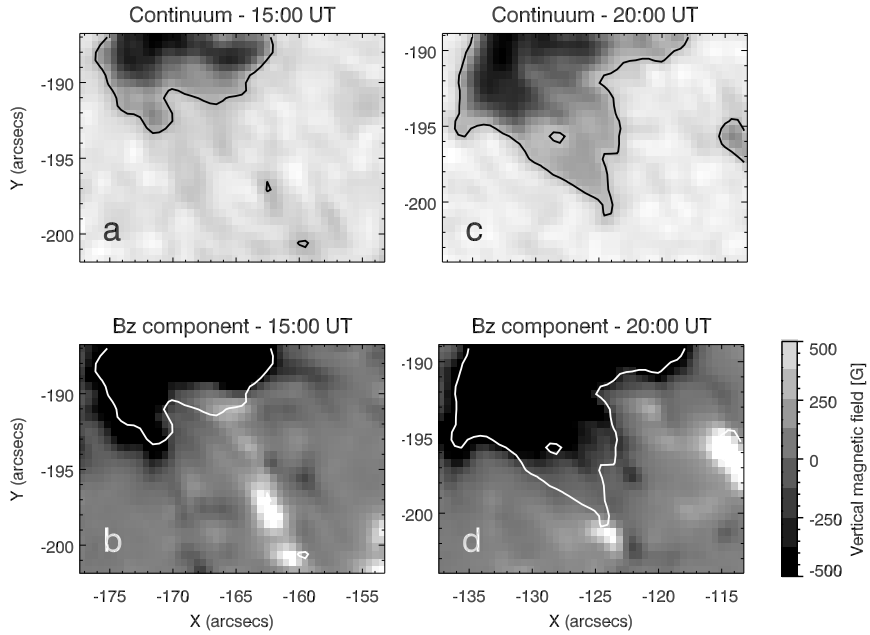


Figure 5.2: Maps of the continuum intensity and of the vertical magnetic field, (a,b) at 15:00 UT and (c,d) at 20:00 UT, respectively. Values of the vertical magnetic field are saturated at ±500 G. Black (white) contour indicate the area characterized by $I_c$=0.9.

Figure 5.1(d) shows that the first penumbral filaments are already formed at 18:00 UT. These filaments increase radially in size, outward from the spot and toward the opposite polarity. Figures 5.2 and 5.3 show the results obtained from the analysis of the region around the first penumbral sector. This analysis clarifies that these filaments are stable. In fact, this region, indicated with the red box in Figure 5.1(a), was analyzed in more detail using the vertical component of the magnetic field deduced from HMI data, from 14:00 UT to 21:00 UT. In Figure 5.2(a), at 15:00 UT it can be seen the presence of some dark areas with $0.5 < I_c < 0.9$. The large area located at [-175″,-165″]×[-193″,-188″] is characterized by negative polarity (Figure 5.2(b)), the same as the adjacent pore. There is also a dark patch with positive field facing the pore at [-164″,-159″]×[-201″,-196″] (see Figure 5.2(b)). However, at 20:00 UT the latter disappears, while the dark area with negative field adjacent to the pore increases, as can be seen from Figure 5.2(c)-(d). Figure 5.3(e) reports the positive (red symbols) and negative (blue symbols) magnetic flux evolution in the areas with $0.5 < I_c < 0.9$, corresponding to the regions of penumbra formation included in the red box. The simultaneous evolution of the spatial extent of these areas is also reported in Figure 5.4(f). These plots illustrate that the first penumbral sector grows smoothly without interruption as the negative magnetic flux increases. This trend remains constant after 21:00 UT. In contrast, the penumbral areas characterized

by positive magnetic field are transient.

The high resolution data acquired by IBIS (FOV A and FOV B indicated in Figure 4.1) are shown in Figure 5.4. In particular, the top panels display the maps acquired in the continuum of the Fe I 617.3 nm and in the center of the Ca II 854.2 nm line on May 28. The bottom panels show the magnetic field strength and the inclination angle obtained from the SIR inversion of the Fe line. These images were obtained using a cross-correlation technique aligning a common area between the two FOVs.

The region between the two polarities at [-170″,-150″]×[-225″,-205″] is characterized by elongated granules (see the top left panel of Figure 5.4). The map in the Ca II line exhibits an AFS in the same region, suggesting that this region corresponds to a region of magnetic flux emergence. It is possible to note a filamentary shape, with a sea-serpent configuration, i.e. formed by a bundle of bipolar patches (e.g. Sainz Dalda & Bellot Rubio, 2008), in the magnetic field map (bottom left panel of Figure 5.4). Moreover, these filamentary structures are not aligned with the AFS visible in chromophere. The inclination of the magnetic field map reveals similar filamentary and mixed pattern but on a larger scale (see the bottom right panel of Figure 5.4). In fact, the magnetic field inclination in the filaments is found to be both smaller and larger than 90°.

Figure 5.5 shows the linear and circular polarization maps relevant to FOV B deduced by IBIS spectropolarimetric data

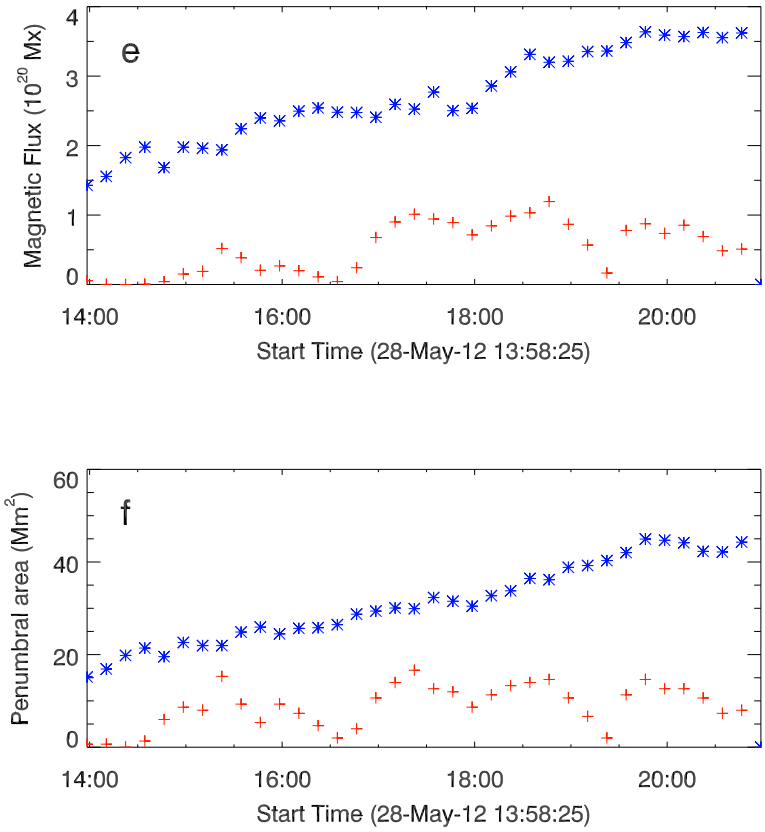


Figure 5.3: Plots of the magnetic flux (e) within the penumbral area and (f) of the total penumbral area included in the red box shown in Figure 5.1. Red (blue) symbols refer to positive (negative) areas. Positive values are amplified by a factor of 5 for a better visualization.

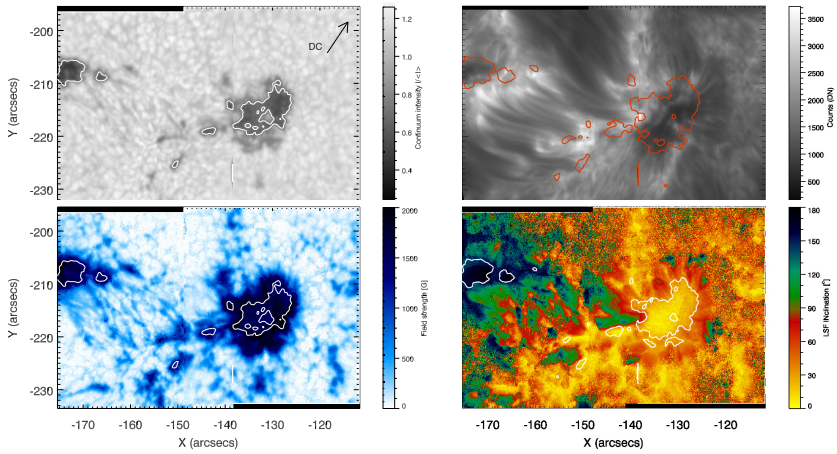


Figure 5.4: Maps of the continuum intensity at the Fe I 617.3 nm line (top, left panel), of the intensity in the center of the Ca II 854.2 nm line (top, rigth panel) on 2012 May 28 at around 14:30 UT from IBIS data. Maps of the magnetic field strength and of the inclination angle obtained from the SIR inversion of the Stokes profiles along the Fe I 617.3 nm line acquired by IBIS. The contours indicate the edge of the pore at $I_c = 0.8$.

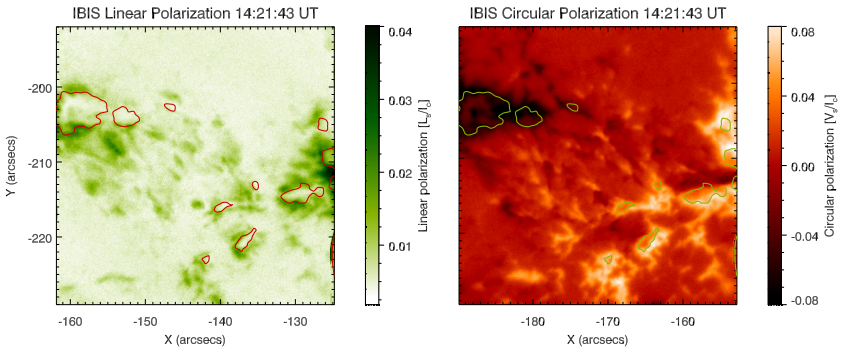


Figure 5.5: Maps of mean linear and circular polarization signals, $L_s$ (left) and $V_s$ (right), obtained from IBIS data for FOV B. Red and green contours indicate the edge of the pore at $I_c = 0.8$.

at 14:21 UT, i.e., the scan acquired during the best seeing conditions. From these maps, it is possible to recognize the same filamentary structure already described in Figure 5.4. $L_s$ map (left panel of Figure 5.5) reveals a wide region at [-210″,-205″]×[-162″,-152″] around the protospot, with different values of linear polarization. The region where later the first penumbral filaments appear is characterized by a value of $L_s$ larger than 4%, while in the northern part of the pore it is smaller than 1%. The area of the proto-spot is also characterized by a diffuse negative polarity, as it can be seen in the circular polarization map $V_s$, (right panel of Figure 5.5). This map reveals a magnetic pattern characterized by alternate positive and negative bipoles between the two polarities, with a sea-serpent configuration.

# Chapter 6

# Penumbra formation in a sample of active regions

In this chapter I describe a study performed over a sample of six ARs to better investigate two aspects concerning the penumbra formation: the location of the stable settlement of the penumbra – whether it occurs between the two opposite magnetic polarities, or on the opposite side – and the transition from inverse Evershed flow to classical Evershed flow.

## 6.1 Observations and Analysis

The selected ARs of this study are listed in Table 6.1. The second column provides the FOV center position of the entire AR at the beginning of the observations, the third and fourth

columns provide the time of the beginning and end of the observations. The end time indicates the time at which the stable penumbra completed its formation process.

Space weather HMI AR patches continuum filtergrams, LOS magnetograms, Dopplergrams taken by HMI along the Fe I 617.3 nm line with a resolution of 1″, a cadence of 12 minutes and a pizel size of 0.″5 were used.

Table 6.1: Selected Active Regions

| AR | Position [arcsec] | Start Time (UT) | End Time (UT) |
|---|---|---|---|
| 11466 | (-600, 270) | 2012/04/22 03:00 | 2012/04/22 23:00 |
| 11512 | (750, -280) | 2012/06/25 01:00 | 2012/06/28 00:00 |
| 11554 | (-380, 150) | 2012/08/24 06:00 | 2012/08/25 21:00 |
| 11610 | (-520, -440) | 2012/11/09 15:00 | 2012/11/11 06:00 |
| 11630 | (-250, 310) | 2012/12/09 00:00 | 2012/12/10 00:00 |
| 11640 | (-410, 490) | 2012/12/30 10:00 | 2013/01/03 10:00 |

The following criteria were used to select these six ARs, observed on 2012 during the maximum of solar cycle 24:

- penumbra formation occurring while the sunspots of the ARs were visible on the solar disk;

- $\beta$-type magnetic field configuration during the entire passage of the AR over the visible solar hemisphere.

I calibrated the LOS velocity assuming that, on average, there is no plasma motion in the umbra (Rimmele, 1994). Therefore, I calculated the mean velocity in the umbra, defined with a threshold of the normalized continuum intensity $I_c < 0.5$, and I subtracted it from the velocity in each pixel of the FOV.

## 6.2 Location of the first penumbra sectors

---

All ARs follow the Hale's law (Hale & Nicholson, 1925). The continuum intensity maps and the simultaneous magnetograms of the selected ARs at the beginning of the observation are shown in Figure 6.1. The protospots of the selected ARs were classified as A, B or X depending on the side where the first stable penumbral sector forms. As a criterion to determine the stability of the penumbral filaments I considered that a sector of the penumbra was stable when its lifetime was 10 times longer than the granular lifetime, following Schlichenmaier et al. (2010). Then, an AR was labelled with A when the first stable penumbral sector forms away from the opposite polarity (see the top panel of Figure 6.2). I indicated with B those ARs where the penumbra starts to form between the two main polarities (see Figure 6.2, bottom

Table 6.2: Properties of the selected ARs.

| AR | Polarity[1] | Class[2] | Time [hr] | Penumbra development[3] | Inverse Evershed flow |
|---|---|---|---|---|---|
| NOAA | F | X | - | - | - |
| 11466 | P | B | 8 | C | Yes |
| NOAA | F | B | 12 | I | Yes |
| 11512 | P | A | 71 | C | Yes |
| NOAA | F | A | 8 | I | No |
| 11554 | P | B | 17 | C | No |
| NOAA | F | B | 24 | C | Yes |
| 11610 | P | B | 20 | I | No |
| NOAA | F | A | 10 | C | Yes |
| 11630 | P | A | 6 | C | Yes |
| NOAA | F | - | 60 | I | No |
| 11640 | P | A | 55 | C | Yes |

[1] P : preceding spot; F : following spot.
[2] A : first penumbral sector forms away from the opposite polarity; B : first penumbral sector forms in the region between the two polarities; X : no penumbra forms during the observations.
[3] C : complete penumbra; I : penumbral sectors.

panel). Finally, X indicates that no penumbra forms during the observing time. Table 6.2 reports this information in the third column. The fourth column of Table 6.2 lists the time interval needed for the penumbra formation (in hours). The fifth column reports whether the pore forms a complete penumbra reaching the condition of a mature sunspot. The sixth column reports the presence of the inverse Evershed flow before the penumbra formation.

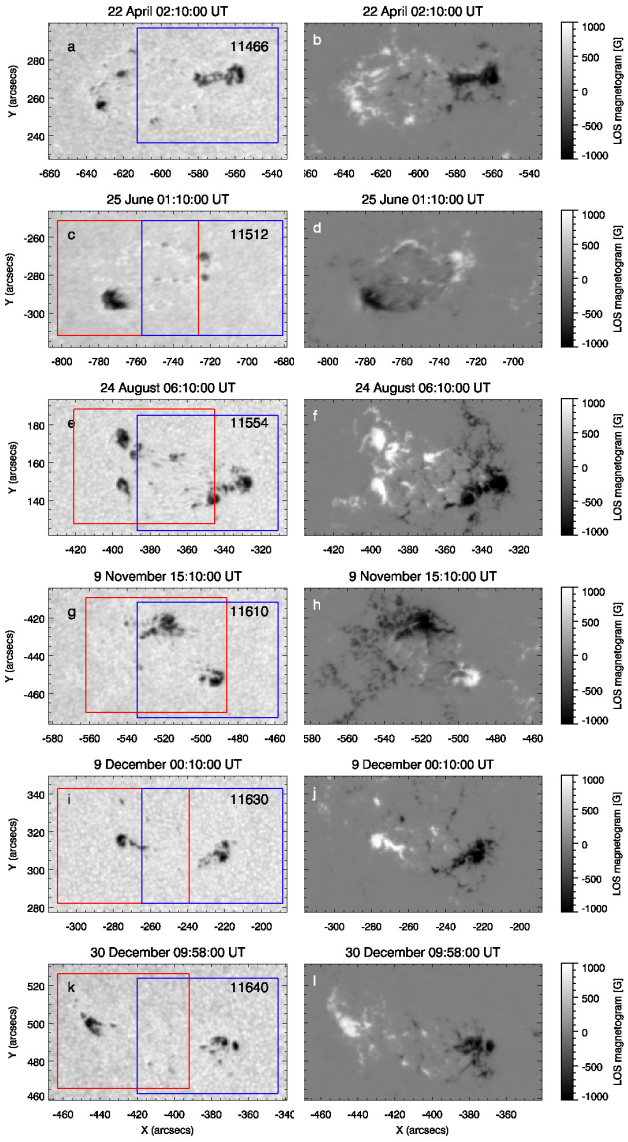


Figure 6.1: Continuum filtergrams (left column) and LOS magnetograms (rigth column) of the ARs at the beginning of the observation time. The red and blue boxes indicate the FOVs displayed in the following figures for the following and the preceding polarity, respectively. In all the Figures solar West is on the right, North is on the top.

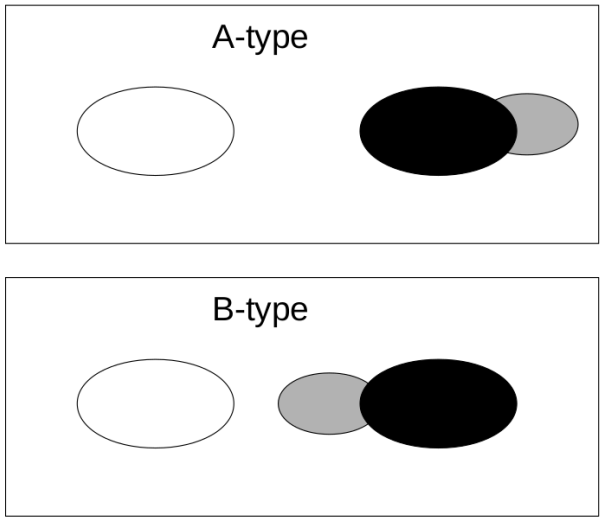


Figure 6.2: Representation of the criteria used to classify the penumbra formation for the selected ARs. White and black oval represent the following and preceding protospots, respectively. The grey oval represents the first penumbral sector.

### AR 11466

The continuum intensity maps and the magnetograms of this AR are shown in Figure 6.1(a)-(b) , at a time when no penumbra was still formed. The AR it is characterized by a widespread ($60'' \times 60''$) positive polarity and a more compact negative polarity. Focusing on the positive polarity, it is possible to note that even if there are two pores relatively close to each other, they do not form a penumbra. Only the negative polarity forms the penumbra, as shown in Figure 6.3. The arrow in Figure 6.3(b) shows the area where the first stable penumbral sector forms, 6 hrs after the beginning of the observations. For about 8 hours the negative magnetic flux continues to coalesce, suggesting that this case of penumbra formation can be ascribed to an active accumulation of magnetic field. It is possibile to see the fully developed and almost symmetric penumbra in the continuum map of Figure 6.3(e).

Taking into account the classification described above, the following spot is an X-type spot, while the preceding one is a B-type spot.

### AR 11512

Panels (c) and (d) of Figure 6.1 show the AR covering an area of $60'' \times 60''$. At the beginning of the observations AR 11512 is composed by a negative pore in the following polarity and some smaller positive pores in the preceding polarity. Figure 6.4 shows

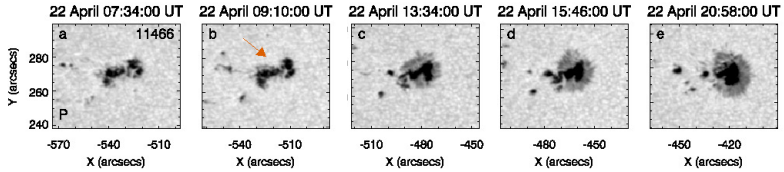


Figure 6.3: Evolution of the penumbra in the continuum maps of the preceding polarity of AR 11466. The following polarity is not shown because it does not form the penumbra. Here and in the following figures, the arrows point the region where the penumbra starts to form.

the evolution of the preceding and following parts of the AR. In particular, after 4 hours from the beginning of the observations, the negative following pore starts to form the penumbra on the side toward the opposite polarity (see Figure 6.4(a)). Red and blue boxes in panels (a)-(e) of Figure 6.4 show that the penumbra formation process for the following polarity is the result of active accumulation and rapid emergence of magnetic flux. In this respect, it is possibile to see a new emerged structure with the same polarity of the main spot, that after 20 hours from the beginning of the observations merges with the main spot (see inside the blue box of Figure 6.4(c)-(d)). However the following polarity is never encircled by a fully developed penumbra. In fact, in Figure 6.4(e) one can see that the penumbra is present only in the northern part of the following polarity.

After 18 hours from the beginning of the observations, the first stable penumbral sector appears also in the positive preced-

ing spot on the side away from the opposite polarity (see Figure 6.4(g)). Panels (f)-(j) of Figure 6.4 show that the formation process can be attributed to active accumulation of magnetic flux. This process lasts for 72 hours and finishes when the penumbra sourronds the pore (see Figure 6.4(j)).

In conclusion, in this AR the negative polarity is a B-type spot while the positive one is A-type.

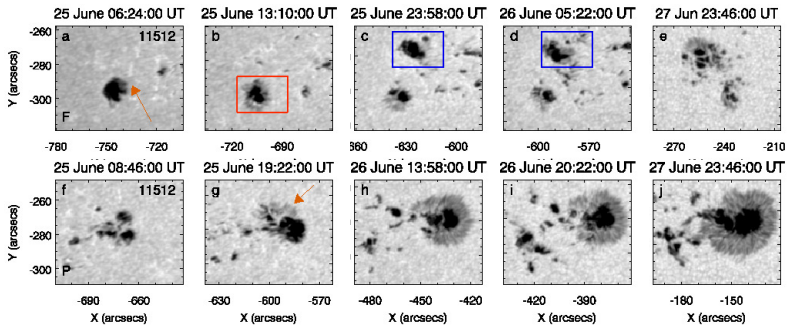


Figure 6.4: Evolution of the penumbra formation in the continuum maps of the following ((a)-(e)) and preceding ((f)-(l)) polarities of AR 11512. Here and in Figures 6.5, 6.6, 6.7, 6.8 coloured boxes indicate the observed different ways of penumbra formation according to Kitai et al. (2014): active accumulation of magnetic fields (red), rapid emergence of magnetic field (blue) and appearance of twisted or rotating magnetic flux tube (yellow).

### AR 11554

Panels (e)-(f) of Figure 6.1 display the continuum intensity map and the magnetogram of the AR, where it is possible to distin-

guish two main pores and some other smaller ones of positive polarity and a group of negative pores ([-360″,-325″]×[145″,155″]). The evolution of the following polarity shows that the large positive pore on the north and a smaller one merged together (see Figure 6.5(a)-(e)). The arrow in Figure 6.5(b) indicates the area where the first penumbral filaments start to form, i.e. on the side away from the opposite polarity. From the analysis of the magnetograms, I inferred that also the features of positive polarity merge and, therefore, this case of penumbra formation can be ascribed to active accumulation of magnetic field. However, the following spot does not show a complete penumbra as it is possible to see in Figure 6.5(e).

The penumbra formation in the preceding negative polarity is faster. In fact, it is possible to see some penumbral filaments in the region toward the opposite polarity already after 3 hours from the beginning of the observations (see Figure 6.5(f)). Figure 6.5(j) displays an elongated umbra encircled by a fully and developed penumbra: their evolution suggest to ascribe the penumbra formation of this polarity to active accumulation of magnetic field.

Summarizing, the following polarity is classified as B-type and the preceding spot as A-type.

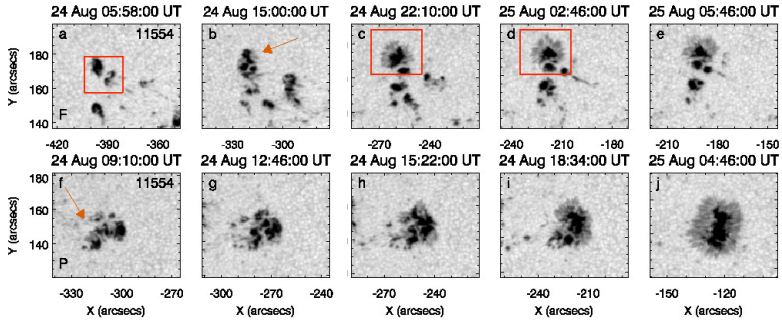


Figure 6.5: Evolution of the penumbra formation in the continuum maps of the following ((a)-(e)) and preceding ((f)-(j)) polarities of AR 11544.

### AR 11610

Panels (g)-(h) of Figure 6.1 display the configuration of the AR 11610 when a small positive polarity and a more diffused negative polarity are present. Concerning the negative polarity, after 2 hours from the beninning of the observations, the first stable penumbral filaments form on the side between the two polarities (see Figure 6.6(a)). The penumbra formation process, shown in Figure 6.6(a)-(e), finishes when a partial penumbra surrounds the umbra after 24 hours of active accumulation of magnetic field (see Figure 6.6(e)).

Due to a rapid emergence of magnetic field, in the preceding spot the penumbra forms in the region toward the opposite polarity, as shown in the blue box in Figure 6.6(f)-(j). At the end

of the formation process, the penumbra encircles the umbra only on the eastern side of the spot (see Figure 6.6(l)).

Summarizing, both polarities are classified as B-type.

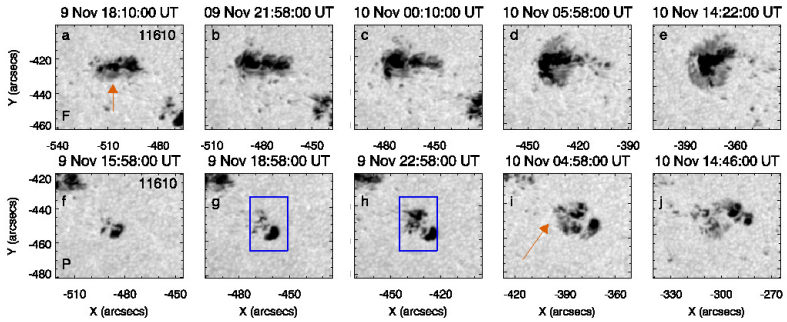


Figure 6.6: Evolution of the penumbra formation in the continuum maps of the following ((a)-(e)) and preceding ((f)-(j)) polarities of AR 11610.

### AR 11630

Figure 6.1(j) displays that in this AR the two polarities are well separated. One can distinguish in the continuum map of Figure 6.1(i) two dark structures with elongated shape and characterized by opposite polarities. Regarding the following polarity, the side where the first stable penumbral filaments start to form, is away from the opposite polarity (Figure 6.7(b)). The penumbral filaments to the northern and western side of the spot are visibly inclined with respect to the radial direction from the umbra center. The yellow box in the panels (a), (c) and (d) of

Figure 6.7, shows clearly that this phenomenon lasts for about 8 hours. Therefore, this process can be ascribed to a different penumbra formation process, where a twisting or rotating magnetic flux tube crosses the photophere. The final stage where a full penumbra surrounds the umbra is visible after about 22 hours in Figure 6.7(e).

Analyzing the evolution of the preceding polarity, one can see after 8 hours from the beginning of the observations, the first penumbral filaments appearing on the side away from the opposite polarity. The evolution of the area inside the red box in Figure 6.7(f)-(j) shows that the formation process is a result of active accumulation of magnetic field. The blue box in Figure 6.7(h)-(j) shows that, since 13:00 UT in the area between the two polarities and near the main preceding spot, new magnetic flux emerges. The umbra is never encircled by a fully developed penumbra (see Figure 6.7(j)).

Both preceding and following polarities are classified as A-type.

### AR 11640

Figure 6.1(k) shows the continuum intensity map of AR 11640. It is characterized by two main pores separated by $\sim 50''$.

The penumbra formation process in the following part of the AR is very long, and during the first day of the observations is not visible any change in the continuum intensity. Three days later

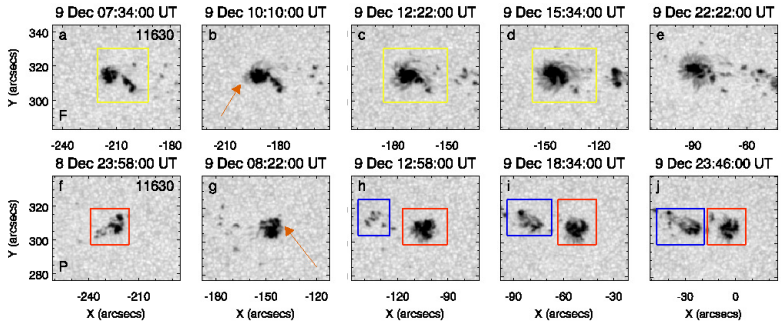


Figure 6.7: Evolution of the penumbra formation in the continuum maps of the following ((a)-(e)) and preceding ((f)-(j)) polarities of AR 11630.

the northern part of a newly structure shows some penumbra filaments (see Figure 6.8(d)). Figure 6.8(e) shows that one day later a fragmented umbra was surrounded by a partial penumbra. It this case it is not possible to distinguish what processes are involved in the penumbra formation.

Concerning the preceding spot, after 12 hours from the beginning of the observations, the first penumbral sector starts to form on the side away from the opposite polarity (see Figure 6.8(g)). Figure 6.8(j) displays a fully developed penumbra surrounding the umbra.

The preceding spot is an A-type spot.

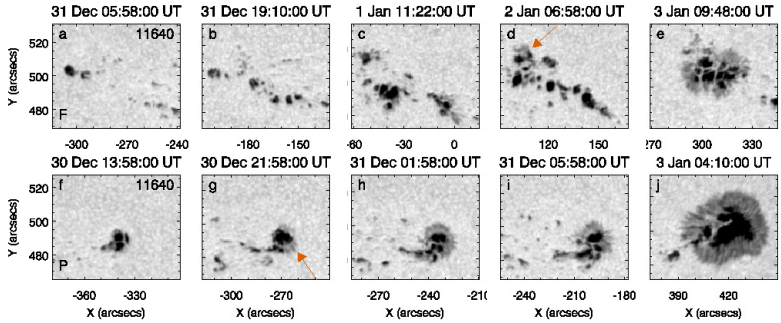


Figure 6.8: Evolution of the penumbra formation in the continuum maps of the following ((a)-(e)) and preceding ((f)-(j)) polarities of AR 11640.

## 6.3 Evolution in the upper atmopheric layers

Figure 6.9 shows the evolution of the preceding polarity of AR 11466 in three EUV channels (304 Å, 171 Å and 335 Å) and in the 1600 Å channel of AIA instrument. In the upper chromophere (see second row, Figure 6.9) it is possible to detect emission in the region between the two polarities. Later, when the penumbra encircles the umbra (at 15:46 UT and 20:50 UT) the emission is visible also in the region away from the opposite polarity. Before the penumbra, formation in the lower corona at 171 Å (see third row, Figure 6.9, [-550″, -530″]×[270″,300″]),

two elongated features are present in the region where successively the penumbra forms. These structures move toward the region away from the opposite polarity (see panel at 13:35 UT), becoming broader. When the penumbra has formed it is possible to note a significant emission on the opposite side. Finally, also the 335 Å EUV channel shows emission in the region between the two polarities, with some coronal arches departing from the region where the penumbra starts to form.

## 6.4 Transition from inverse to classical Evershed flow

Before the penumbra formation, it was possible to detect in some ARs the transition from the inverse Evershed flow to the classical Evershed flow. Figures 6.10 and 6.11 show the continuum intensity and LOS velocity maps of these ARs.

In the black and green boxes of Figure 6.10, it is possible to note that before the formation of the penumbra the flow has a different pattern with respect to the classical Evershed flow shown in panel (h) of Figure 6.10. The evolution of the LOS velocity in the black square (panels (e)-(h) of Figure 6.10) displays that in about 6 hours (from 3:00 Ut to 9:24 UT) the blushifted area in the northern side of the protospot becomes redshifted. The velocity changes from -120 m $s^{-1}$, inside the black square be-

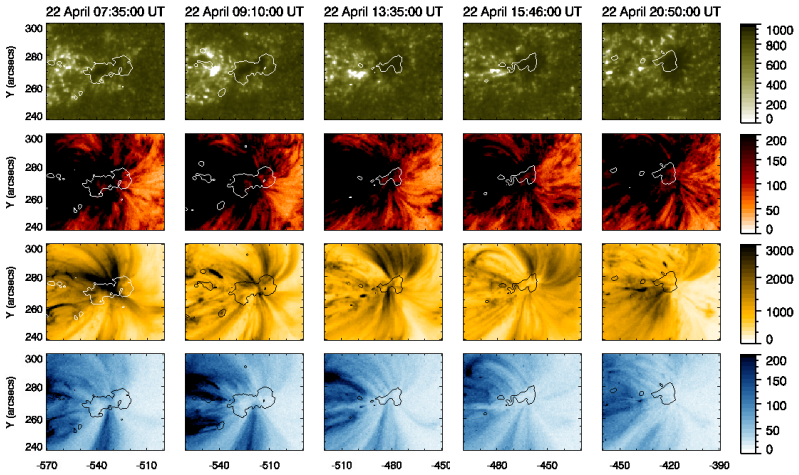


Figure 6.9: Evolution of the preceding polarity of AR 11466 in the 1600 Å channel (first row) and in the EUV channels (304 Å, 171 Å and 335 Å (second, third and fourth row). The black and white contours in all panels indicate the edge of the pore at $I_c$=0.9 (at 07:34 UT and 09:10 UT, before the penumbra formation) and $I_c$=0.6 (13:35 UT, 15:46 UT and 20:50 UT, after the penumbra formation). All the EUV maps (second, third and fourth row) are shown in reverse intensity scale. The intensity values are given in data-number units.

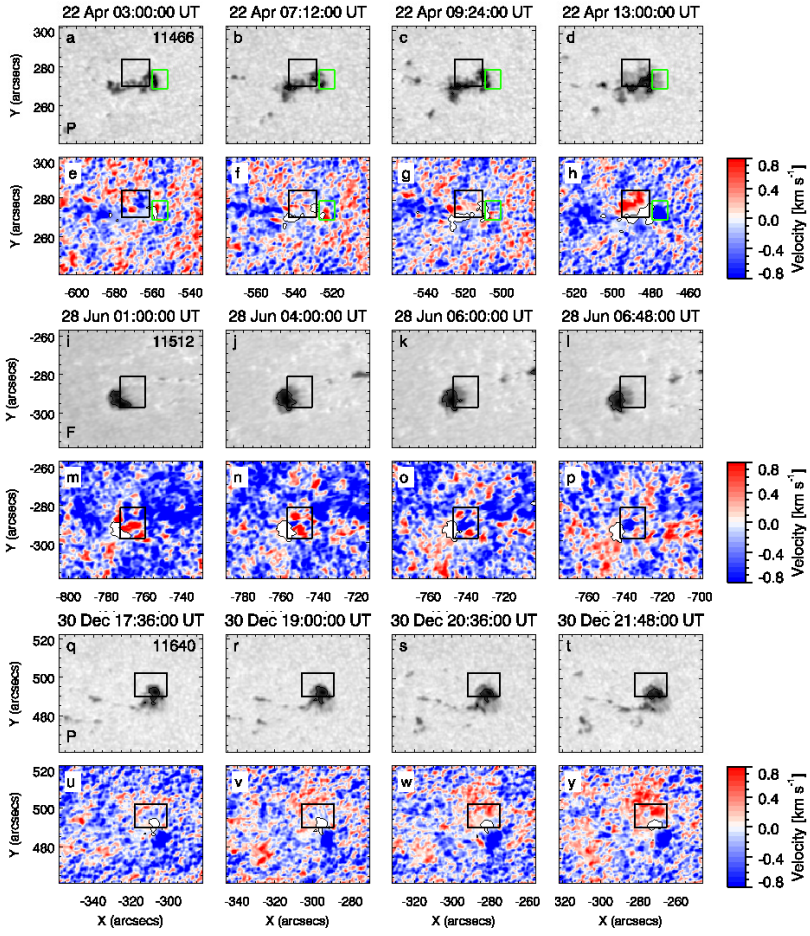


Figure 6.10: From top to bottom: zoom of the continuum and LOS velocity maps of the preceding sunspot of AR 11466((a)-(h)), of the following spot of AR 11512 ((i)-(p)) and of the preceding spot of AR 11640 ((q)-(y)). The boxes in all panels, here and in the next figure, indicate the regions where I calculated the values of the velocity reported in Table 6.2.

Table 6.3: LOS velocity around sunspots

| AR | Initial Velocity [m s$^{-1}$] | Final Velocity [m s$^{-1}$] |
|---|---|---|
| 11466 | Black box: -120 | 300 |
| | Green box: 100 | -540 |
| 11512 | 90 | -250 |
| 11610 | -160 | 210 |
| 11630 | 220 | -260 |
| 11640 | -40 | 230 |

fore the penumbra formation, to 300 m s$^{-1}$ after the penumbra formation. The west side of the protospot of AR 11466 shows an opposite behaviour (see green square in Figure 6.10(a)-(h)). The penumbra in this area is not visible at 7:12 UT (green square in panels (b) and (f) of Figure 6.10) and it is characterized by a downflow of about 500 m s$^{-1}$. After 6 hours, at 13:00 UT (panel (h) of Figure 6.10), the region becomes blushifted with a velocity of about -600 m s$^{-1}$.

The transition from the inverse Evershed flow to classical one is also observed in AR 11512. The area charcaterized by a downflow before the penumbra formation, in the black square of panel (m) of Figure 6.10, decreases and the blushifted area increases

consequently (see Figure 6.10(o)-(p)) in about 6 hours. Figure 6.10 (q)-(y) shows a similar behaviour in the west side of AR 11466. In fact, it is possible to observe a region without penumbra characterized by an upflow that in 4 hours, from 17:36 UT to 21:48 UT, becomes redshifted (downflow) with the appearance of some penumbral filaments.

In Figure 6.11(a)-(h) and (i)-(p), it is possible to note that, although the penumbra formation process has already started, the transition from inverse Evershed flow to classical Evershed flow is clearly visible in AR 11610 and AR 11630. In particular, at 9:34 UT the penumbra encircles almost all the umbra in the AR 11610. There is a sector on the eastern side of the following spot where the penumbra is not present and there it is possible to see the onset of the Evershed flow. When the penumbra is completely formed the mean velocity is around 210 m $s^{-1}$, while 6 hours before its formation the velocity was around -160 m $s^{-1}$. The onset of the Evershed flow on the western side of the following spot of AR 11630 was faster. In fact, in 1 hour the penumbra filaments appear and a transition from redshift to blushift is observed (see Figure 6.11(j) and Figure 6.11(n)).

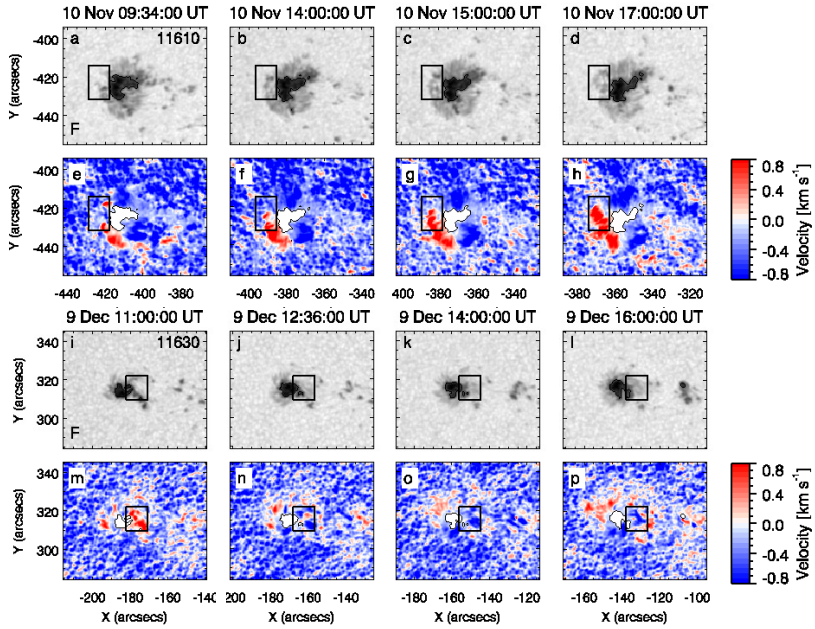


Figure 6.11: Zoom of the continuum and LOS velocity maps of the following sunspot of AR 11610((a)-(h)), of the following sunspot of AR 11630 ((i)-(p)).

# Chapter 7

# Discussion

## 7.1 A possible scenario for the penumbra formation

In Chapter 4 I investigated the penumbra formation and the onset of the Evershed flow in the preceding polarity of the AR NOAA 11490. Following the entire evolution of the AR with SDO/HMI, I observed the first settlement of the penumbra filaments on the north and south of the pore, then in the western and only at the end in the area facing the opposite polarity. This behavior is in agreement with the observations of Schlichenmaier et al. (2010), who noted that the penumbra starts to form in the side away from the opposite polarity.

The analysis of the high resolution data relevant to AR 11490 showed that, before the penumbra formation, the pore exhibits

an annular zone just outside its boundary in the continuum intensity map. This annular zone is characterized by a magnetic field greater than 1000 G, having an (upside down) ballerina skirt structure of the magnetic field. The inner part of the annular zone is characterized by downflow. In particular, I focused my attention on the formation of a penumbral sector where the direction of the LOS velocity field changes in about 1-3 hours, becoming coherent with the Evershed flow pattern when the penumbra is completely formed. I also observed that the magnetic field increases its strength only some minutes after the Evershed-like flow has been estabilished.

To explain the transition from the inverse Evershed flow to the classic one, the presence of small U-loops, formed by the convective flows that drag the field lines down into the photosphere, is assumed (see, e.g., Murabito et al. (2016)). These small U-loops have their inner footpoint polarity opposite to that of the pore and are characterized by weak field (compared to the pore) and this should drive the siphon flow toward the pore. In this way it is possible to explain the observed inverse Evershed flow. Later, the flux in the external footpoint of the inverted U-loop increases, because the flux is dragged down. The increases of the flux has as a conseguence the inihibition of the convection. Then the region darkens until it reaches a new equilibrium and the magnetoconvection starts. At this point the Evershed flow is set up as part of the magnetoconvection process.

## 7.2 Penumbra formation in the region between two opposite polarities

I also analyzed the penumbra formation of the following polarity of the AR NOAA 11490, where the penumbral filaments form on the side facing the opposite polarity. I observed elongated granules in photosphere and an AFS in chromosphere in the area between the two polarities. From these signatures I deduced that the region between the two polarities is characterized by a large amount of emerging magnetic flux. In this case, the observed penumbra formation is not in agreement with the results obtained by Schlichenmaier et al. (2010) who argued that the penumbra cannot form in the area between the two polarities because the strong dynamics introduced by ongoing flux emergence inhibits the settlement of the penumbra.

I also observed in this region a configuration of the magnetic field similar to the sea-serpent configuration. The area where the penumbra starts to form shows the presence of horizontal field before the penumbra formation, in agreement with the recent simulations of MacTaggart et al. (2016). In their simulations, they demonstrated that the overlying magnetic canopies are the source of highly horizontal fields required in the penumbra formation process. The probability to find these canopies is higher in the area away from the opposite polarities, but they found

that there is a non-zero probability of finding near-horizontal field also in the region between the two main sunspots.

## 7.3 Settlement of the first penumbral filaments and their velocity field evolution

---

The penumbra formation in six ARs, has been reported in Chapter 6. I found that in five pores the first stable penumbral sector forms on the side away from the opposite polarity and in five spots on the area between the two polarities. The side where the penumbra starts to form seems to be associated with the time needed for the penumbra formation. In fact, the first stable penumbral filaments on the area facing the opposite polarity appear quicker than those in the area away from the opposite polarity. Therefore, it seems there is no a preferred location for the penumbra formation.

I also found observational evidences of the transition from the inverse Evershed flow to the classic Evershed flow in most of the pores of our sample. In particular, I found that the Evershed flow pattern appears in sectors like the penumbra in about 1-6 hours and it is possible to see the transition from inverse to classic Evershed flow only when the penumbra sector has already formed.

In general, the observed flow before the penumbra formation and the transition from the inverse Evershed flow to the classic one not only could be considered a precursor of the penumbra formation, but also confirm the observations and the scenario proposed in the Section 7.1.

Finally I found that the penumbra can form through different mechanisms as proposed by Kitai et al. (2014), i.e. active accumulation of the magnetic field, rapid emergence of the magnetic field and appearance of twisting or rotating magnetic flux tube. I noted, analyzing only $\beta$ ARs, that not all the mechanisms are included in the formation of a single AR.

# Chapter 8

# Conclusions

In this thesis I studied the physical processes at the base of the sunspot penumbra formation in the solar atmosphere.

I described the theoretical aspects of this process with particular attention to the physical conditions needed to the settlement of the penumbra. Then, I provided some observational contributions to this issue in order to understand the conditions needed for the development of the penumbra.

The most important results are:

i) The first penumbral sectors appear both in the area away from the opposite polarity and in the area between the two polarities. Analyzing six ARs, I found that half of the studied spots form the first stable penumbral sector away from the opposite polarity and half toward the opposite polarity.

ii) A flow of opposite sign with respect to the Evershed flow has been observed, called inverse Evershed flow, before the penumbra formation. The transition from the inverse Evershed flow to the classic one occurs in about 1-6 hours.

Concerning the side where the penumbra starts to form, although previous observations (Schlichenmaier et al., 2010) provided evidence that the preferred side for the penumbra formation should be the area away from the opposite polarity, I found that the penumbra can also appear in the area between the two polarities.

Certainly, analyzing more and more sunspots at high resolution, it could be possible to better understand the physical conditions behind this process. Moreover, a better comprehension of the inverse Evershed flow shall be useful to explain the processes of energy transport in the penumbra where, in principle, the presence of a rather strong (1500 G) and horizontal (40°-80°) magnetic field should inhibit the convective motions.

In conclusion, all of the aspects concerning the penumbra formation need to be investigated in more detail eventually benefitting from the extremely high capability of the next generation of ground-based and space-based telescopes. In addition, it is desirable that future numerical simulations may reproduce the details of this physical process in order to increase our understanding of these phenomena occurring in the solar atmosphere.

# Bibliography

Balthasar, H., 1988, A&A, 72, 473

Bellot Rubio, L. R., Schlichenmaier, R., & Tritschler, A. 2006, A&A, 453, 1117

Bobra, M. J., Sun, X., Hoeksema, J. T., Turmon, M., Liu, Y., Hayashi, K., Barnes, G., Leka, K. D., 2014, Sol. Phys., 289, 3549-3578

Borrero, J. M., & Solanki, S. K. 2008, ApJ, 687, 668-677

Borrero, J. M., & Ichimoto, K. 2011, Living Reviews in Solar Physics, 8, 4

Bruzek, A. 1968, Structure and Development of Solar Active Regions, 35, 293

Cavallini, F. 2006, Sol. Phys., 236, 415

Chen, F., Rempel, M., & Fan, Y. 2017, arXiv:1704.05999

Cheung, M. C. M., Schüssler, M., Tarbell, T. D., & Title, A. M. 2008, ApJ, 687, 1373-1387

Cheung, M. C. M., Rempel, M., Title, A. M., & Schüssler, M. 2010, ApJ, 720, 233

Choudhuri, A. R. 1986, ApJ, 302, 809

Collados, M., Martinez Pillet, V., Ruiz Cobo, B.,Del Toro Iniesta, J.C., & Vzquez, M. 1994 A&A, 291, 622

Cowling T.G., 1957, Magnetohydrodynamics, Interscience, New York

Danielson, R. E. 1961, ApJ, 134, 275

Danielson, R. E. 1964, ApJ, 139, 45

Del Toro Iniesta, J.C., Tarbell, T.D., Ruiz Cobo, B., 1994,ApJ, 436, 400

del Toro Iniesta, J. C. 2003, Introduction to Spectropolarimetry, by Jose Carlos del Toro Iniesta, pp. 244. ISBN 0521818273. Cambridge, UK: Cambridge University Press, April 2003., 244

Dravins, D., Lindergren, L., and Nordlund, Å, 1981, A&A, 96,345

Evershed, J. 1909, The Observatory, 32, 291

Falco, M., Borrero, J. M., Guglielmino, S. L., et al. 2016, Sol. Phys., 291, 1939

Georgoulis, M. K. 2005, ApJ, 629, L69

Gingerich, O., Noyes, R. W., Kalkofen, W., & Cuny, Y. 1971, Sol. Phys., 18, 347

Guglielmino, S. L., Bellot Rubio, L. R., Zuccarello, F., et al. 2010, ApJ, 724, 1083

Hale, G. E. 1908, ApJ, 28, 315

Hale, G. E., & Nicholson, S. B. 1925, ApJ, 62, 270

Harvey, K. L., & Zwaan, C. 1993, Sol. Phys., 148, 85

Heinemann, T., Nordlund, Å., Scharmer, G. B., & Spruit, H. C. 2007, ApJ, 669, 1390

Ichimoto, K., Shine, R. A., Lites, B., et al. 2007, Publications of the Astronomical Society of Japan, 59, S593

Jiang, J., Cameron, R. H., Schmitt, D., & Schüssler, M. 2011, A&A, 528, A82

Jurcak, J., 2011, A&A, 531, A118

Jurcak, J., Bello González, R., Schlichenmaier, R., and Rezai, R., 2011, A&A, 580, L1

Kawai, G., Kurokawa, H., Tsuneta, S., et al. 1992, Publications of the Astronomical Society of Japan, 44, L193

Kitai, R., Watanabe, H., & Otsuji, K. 2014, Publications of the Astronomical Society of Japan, 66, S11

Landi Degl'Innocenti, E. 1983, Sol. Phys., 85, 3

Landi Degl'Innocenti, E., & Landi Degl'Innocenti, M. 1985, Sol. Phys., 97, 239

Landi Degl'Innocenti, E. 2008, Springer

Leka, K. L. 1997, ApJ, 484, 900

Leka, K.D., & Skumanich, A. 1998, ApJ, 507, 454

Lemen, J. R., Title, A. M., Akin, D. J., et al. 2012, Sol. Phys., 275, 17

Lites, B. W., Skumanich, A., & Martinez Pillet, V. 1998, A&A, 333, 1053

Lim, E., Yurchyshyn, V., Goode, P. & Cho, K. 2013, ApJ, 769, L18

Löfdahl, M.G. 2002, SPIE, 4792, 146L

MacTaggart, D., Guglielmino, S. L., & Zuccarello, F. 2016, ApJL, 831, L4

Malherbe, J. M., Schmieder, B., Mein, P., et al. 1998, Sol. Phys., 180, 265

Meyer, F., & Schmidt, H. U. 1968, Mitteilungen der Astronomischen Gesellschaft Hamburg, 25, 194

Muller, R. 1973, Sol. Phys., 32, 409

Murabito, M., Romano, P., Guglielmino, S. L., Zuccarello, F., & Solanki, S. K. 2016, ApJ, 825, 75

Murabito, M., Romano, P., Guglielmino, S. L., & Zuccarello, F. 2017, ApJ, 834, 76

Parker, E. N. 1978, ApJ, 221, 368

Parker, E. N. 1979a, ApJ, 230, 905

Parker, E. N. 1979b, ApJ, 230, 914

Parker, E. N. 1979c, ApJ, 231, 250

Petrovay, K., & van Driel-Gesztelyi, L. 1997, Sol. Phys., 176, 249

Pesnell, W. D., Thompson, B. J., & Chamberlin, P. C. 2012, Sol. Phys., 275, 3

Reardon, K. P., & Cavallini, F. 2008, A&A, 481, 897

Rempel, M., Schüssler, M., & Knölker, M. 2009a, ApJ, 691, 640

Rempel, M., Schüssler, M., Cameron, R. H., & Knölker, M. 2009b, Science, 325, 171

Rempel, M. 2011a, ApJ, 729, 5

Rempel, M., & Schlichenmaier, R. 2011, Living Reviews in Solar Physics, 8, 3

Rempel, M. 2012, ApJ, 750, 62

Rempel, M., & Cheung, M. C. M. 2014, ApJ, 785, 90

Rezaei, R., Bello González, N., & Schlichenmaier, R. 2012, A&A, 537, A19

Rimmele, T. R. 1994, A&A, 290, 972

Romano, P., Frasca, D., Guglielmino, S.L., Ermolli, I., Tritschler, A., Reardon, K. P., & Zuccarello, F. 2013, ApJ, 771, L3

Romano, P., Guglielmino, S.L., Cristaldi, A., Ermolli, I., Falco, M., & Zuccarello, F. 2014, ApJ, 784, 10

Ruiz Cobo, B., & del Toro Iniesta, J. C. 1992, ApJ, 398, 375

Sainz Dalda, A., & Bellot Rubio, L. R. 2008, A&A, 481, L21

Scharmer, G. B., Gudiksen, B. V., Kiselman, D., Löfdahl, M. G.

Scherrer, P. H., Bogart, R. S., Bush, R. I., et al. 1995, Sol. Phys., 162, 129

Scherrer, P.H., Schou, J., Bush, R.I., et al. 2012, Sol. Phys., 275, 207

Schlichenmaier, R. 2002, Astronomische Nachrichten, 323, 303

Schlichenmaier, R., Bellot Rubio, L. R., & Tritschler, A. 2005, Astronomische Nachrichten, 326, 301

Schlichenmaier, R., Rezaei, R., Bello González, N., & Waldmann, T. A. 2010, A&A, 512, L1

Schlichenmaier, R., Rezaei, R., & González, N. B. 2012, 4th Hinode Science Meeting: Unsolved Problems and Recent Insights, 455, 61

Schmidt, W., & Balthasar, H. 1994, A&A, 283, 241

Schrijver, C. J., & Zwaan, C. 2000, Cambridge Astrophysics Series, 34,

Schüssler, M., & Vögler, A. 2006, ApJL, 641, L73

Sheeley, N. R., Jr. 1981, Solar Active Regions: A monograph from Skylab Solar Workshop III, 17

Shimizu, T., Ichimoto, K., & Suematsu, Y. 2012, ApJL, 747, L18

Sobotka, M., & Puschmann, K. G. 2009, A&A, 504, 575

Solanki, S. K., & Montavon, C. A. P. 1993, A&A, 275, 283

Solanki, S. K. 2003, Astronomy and Astrophysics Reviews, 11, 153

Sütterlin, P., Bellot Rubio, L. R., & Schlichenmaier, R. 2004, A&A, 424, 1049

Spruit, H. C., & Scharmer, G. B. 2006, A&A, 447, 343

Thomas, J. H. 1988, ApJ, 333, 407

Thomas, J. H., & Weiss, N. O. 1992, NATO Advanced Science Institutes (ASI) Series C, 375

Thomas, J. H., & Montesinos, B. 1993, ApJ, 407, 398

Thomas, J. H., Weiss, N. O., Tobias, S. M., & Brummell, N. H. 2002, Nature, 420, 390

Thomas, J., Weiss, N., 204, A&A, 42, (1), 517-54

Tortosa-Andreu, A., & Moreno-Insertis, F. 2009, A&A, 507, 949

Unno, W. 1956, Publications of the Astronomical Society of Japan, 8, 108

van Driel-Gesztelyi, L., & Green, L. M. 2015, Living Reviews in Solar Physics, 12, 1

Watanabe, H., Kitai, R., Okamoto, K., et al. 2008, ApJ, 684, 736-746

Wang, J., Yan, X., Qu, Z., Xue, Z., & Yang, L. 2017, ApJ, 839, 128

Zwaan, C., Brants, J. J., & Cram, L. E. 1985, Sol. Phys., 95, 3